國 立 交 通 大 學

光 電 工 程 研 究 所

碩 士 論 文

金屬光子晶體應用於兆赫輻射控制之研究

Metallic Photonic Crystals for Controlling Terahertz Radiation

研 究 生：王 之 揚

指 導 老 師：潘 犀 靈 教授

中 華 民 國 九 十 三 年 七 月

金屬光子晶體應用於兆赫輻射控制之研究

Metallic Photonic Crystals for Controlling Terahertz Radiation

研究生： 王之揚 Student: Chih-Yang Wang

指導老師：潘犀靈 教授 Advisor: Prof. Ci-Ling Pan

國立交通大學

光電工程研究所

碩士論文

A Dissertation
Submitted to Institute of Electro-Optic Engineering
College of Electrical Engineering and Computer Science
National Chiao Tung University
In partial Fulfillment of the Requirements
for the Degree of
Master of Engineering

August 2004
Hsinchu, Taiwan, Republic of China

中 華 民 國 九 十 三 年 八 月

摘要

由於金屬在兆赫波段 (10^{12} 赫茲) 具有極小而可忽略的吸收，利用金屬來製作適用於兆赫波段的光子晶體結構是一個相當好的選擇。此種結構是利用低成本並容易取得的不銹鋼材料(SUS-304)，經由雷射加工的方式來產生具三角形排列之週期性圓孔的金屬光子晶體。利用兆赫時域光譜技術來量測樣品的穿透光譜，當兆赫波正向入射晶體時，我們發現禁止能帶和允許能帶的出現，此即為預期中的光子晶體現象，我們也報導利用相同結構的鋁合金光子晶體結果，他們的光譜特性與理論預期結果相符。然而對於不同的偏振態入射並不影響穿透光譜，即穿透光譜與偏振態無關，此亦為預期中的現象。另外近年來由於在表面電漿造成異常穿透提升的研究蓬勃發展，我們藉由在晶體表面貼上薄膜膠帶的方式來探討金屬光子晶體的兩側介質對穿透異常提升的影響。最後我們利用兩片晶體製作成具有特定間距的共振腔，發現會使得穿透峰更顯得陡峭，此可歸類於法布禮–派羅效應的影響。

Abstract

Owing to negligible loss of metals in THz region, metals are good candidates for photonic crystals. Metallic photonic crystals with a periodical triangular array of circular holes were fabricated in THz region. The structures were made of low-cost, easily available stainless steels (SUS-304), and an array of holes was drilled by laser cutting. Using THz time-domain spectroscopy to obtain transmission spectra, phenomena of allowed and forbidden bands similar to photonic band gaps appeared when waves were normally incident, and the band can be well defined by Chen's theory. This was also observed using the same structure of aluminum alloy crystals. The same spectra with varying polarizations of a normal incident THz wave ware found. It showed polarization independence. Then extraordinary transmission due to surface plasma effects by attaching tapes to crystals was explored. Finally, a Fabry-Perot etalon of two crystals with specific spacing was made. The sharper transmission peak caused by etalon effects was observed.

Acknowledgement (誌謝)

在風城六年的歲月，每當遇到鳳凰花開總會看到學業完成的歡笑和不捨離別的淚水。然而今年的鳳凰花似乎開的特別艷麗卻也凋謝的特別迅速，花開花落間猶如述說著轉眼的起始與結束。

緣分看似這樣神奇，儘管在歷經波折後，緣分再度牽引著我來到這裡與潘老師相遇，這段日子不只從老師身上學到在專業上的新知與技術，也得到許多經驗的傳承。此外趙如蘋、黃衍介、黃中垚、林恭如等老師對於我在觀念上的釐清與思考上的激發，讓整個研究探討具有新的思維與方向並且更加地完備。

實驗室中引領我進入 THz 領域的宗儒學長，常常會互相討論的老劉，提供歡笑與ㄟ波報的 Chuck，曾經教我許多的炯翰、博文、銘杰、素圓，提供良好雷射使用的 Moya、給予製作樣品建議的 Mika，研討 THz 的昭遠，一起學習討論的嗣文、威宏、建宏、宗盛和世軒，共同努力打拼且互相鼓勵的六位可愛同學，沛霖、秉其、學智、龍進、奕帆和駐外代表怡瑱，還有七個既搞笑又令人感動的學弟，羅誠、小冷、cc、宗瀚、澎湖仔、弘倫和小高，特別是羅誠在最後陪我熬夜實驗卻因此流鼻血的鼎力相助，另外汎怡這些日子的照護以及激勵使我成長許多，育甫、昱宏、及大學和之前好朋友們的幫忙與陪伴，因為你們的支持與鼓勵讓我渡過許多的低潮並減輕相當多的負擔。

然而最重要的依靠來自父母與家人無悔的付出與支持，讓我有安穩的靠山和大步向前的勇氣。由於大家的存在豐富了我的人生，你們的鼎力支持與幫忙，使我每一步都踏的安穩，一步一步穩定成長並努力向前。如今這個階段宣告終了，在此將這份榮耀獻給我的父母，誠摯感謝你們並將喜悅與你們一同分享。

因為有你：

回憶在此萌芽卻在心底深根

即便像風一般瀟灑仍會帶走一絲思念

攜著你的祝福追逐人生夢想

踏上穩健的腳步開創另一個嶄新開始

竹　夢　人
之　揚
2004 夏　于　風　城

Contents

List of Figures and Tables

1. Introduction

The terahertz region of the electromagnetic spectrum ranges from frequencies of about 300 GHz to 10 THz (10 x 10^{12} Hz) as shown in Fig. 1.1. This corresponds to wavelengths between about 1 and 0.03 mm, and lies between the microwave and infrared regions of the spectrum. At lower frequencies, microwaves and millimeter-waves can be generated by "electronic" devices such as those found in mobile phones. At higher frequencies, near-infrared or visible light is generated by "optical" devices such as semiconductor laser diodes, in which electrons emit light when they jump across the semiconductor band gap. Unfortunately, neither electronic nor optical devices can conveniently be made to work in the terahertz region because the terahertz frequency range sits between the electronic and optical regions of the electromagnetic spectrum.

In the past, only Fourier Transform InfraRed (FTIR) spectroscopy is a method in this region, but the lack of brightness of incoherent sources and of functions to measure the real and imagine parts of response functions at a certain frequency are its weaknesses. Therefore, the development of terahertz spectroscopy has been hindered without suitable tools. This situation changed in the 80's with the advent of ultrashort

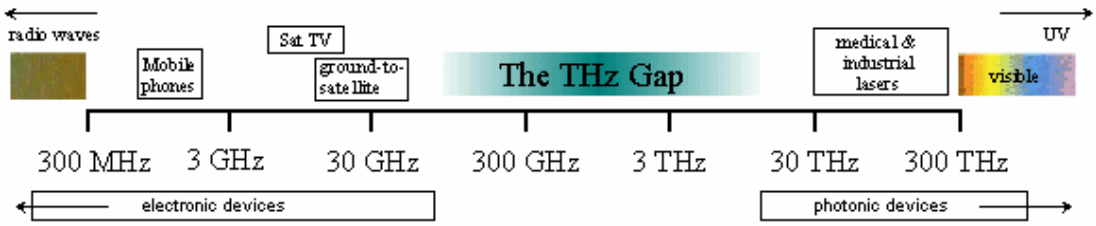

Fig. 1.1 Electromagnetic spectrum

http://www.frascati.enea.it/THz-BRIDGE/

pulse lasers of ~100 fs pulse duration. Ultrashort pulses can generate broadband THz radiation when they impinge on semiconductors. Mourou and Auston [7-8] first demonstrated generation and detection of pulsed THz radiation by photoconducting switch with advantages of time resolution of picosecond and sensitivity enhanced by phase-lock technique. In 1996, Zhang et al. [9] developed free-space electro-optic sampling (FS-EOS) technique to enhance signal to noise ratio (S/N ratio) up to 10000 and to achieve much large dynamic range. These techniques have now developed to a level for spectroscopy and sensing. The spectroscopic technique using pulsed THz radiation is called “THz time-domain spectroscopy (THz-TDS)”.

In the real world, the region is of great importance to the spectroscopy of condensed matter; for example, the electronic properties of semiconductors and metals are much affected by the bound states whose energies fall in the terahertz frequencies. It can show the information of matters, which light at other frequencies can’t observed.

On the other hand, during past few decades, photonic crystals have attracted a great lot of researchers’ interests and had much great development in visible region. Because of the existence of forbidden gaps for electromagnetic waves, they can have an important impact on science and technology. However, one kind of photonic crystals is made of metals, Metallic Photonic Crystals (MPCs). They can have similar characteristics of corresponding dielectric photonic crystals but more compact and lighter [1]. Besides, since the absorption of metals in THz region can be largely negligible [1], MPCs are good candidates for THz applications. Until now, some devices based on MPCs in THz region have been

explored, for example, phase shifter [2], wave plate [3], filters [4], magnetic left-handed materials [5], etc. To meet the requirement of popular THz components in the future, more low-cost, multi-functional, and tunable devices are needed.

In recent years, Ebbesen et al. [6] explored extraordinary transmission of light in optical frequencies through a metal film perforated by an array of sub-wavelength holes. Many researchers have paid much great concentration on this field. However, theories to describe this phenomenon are still ambiguous. Therefore, the purpose of this thesis is to begin new explorations and to make new THz components in THz field.

2. Terahertz Field and Metallic Photonic Crystals

Methods of THz radiation produced by fs laser are commonly and easily used. This chapter describes mechanisms of generation and detection of THz radiation. Finally, theories of metallic photonic crystals used to calculate transmission spectra are chosen.

2.1 Principles of Optically Excited and Detected THz Radiation and its Applications

A popular method to generate or detect THz radiation is using photoconductive (PC) antennas or electro-optic (EO) materials illuminated with fs laser pulses. Using EO materials can produce broader bandwidth THz radiation but the efficiency of energy conversion is great low. In the following sections, their mechanisms are introduced.

2.1.1 Generation of THz Radiation Using PC Antennas

When a femtosecond (fs) laser excites a biased semiconductor with photon energies greater than its bandgap, electrons and holes are produced at the illumination point in the conduction and valence bands, respectively. An electromagnetic field radiating into free-space with the help of an antenna is produced by the fast changes of the density of photocarriers and their acceleration due to the applied dc bias (V_b). The production of ultrashort currents with a full-width half-maximum (FWHM) of 1ps or less strongly depends on the carrier lifetime in the semiconductor. [10]

The carrier density behavior in time is given by

$$dn/dt = -n/\tau_t + G(t) \qquad (2.1)$$

where n is the carrier density and $G(t) = n_0 \exp(t/\Delta t)^2$ is the generation rate of carriers due to laser pulse excitation, with Δt the laser pulse width and n_0 the generated carrier density at t = 0. The generated carriers are accelerated by the electric field bias with a velocity rate given by

$$dv_{e,h}/dt = -v_{e,h}/\tau_{rel} + (q_{e,h}E)/m_{eff,e,h} \quad (2.2)$$

where $v_{e,h}$ are the average velocity of the carrier, $q_{e,h}$ are the charge of the electron and hole, τ_{rel} is the momentum relaxation time, and E is the local electric field, which is less than the applied bias E_b due to the screen effect of space charges. More precisely,

$$E = E_b - P/3\varepsilon_r \quad (2.3)$$

where ε_r is the dielectric constant and $\boldsymbol{P}$ is the polarization induced by the separation of electrons and holes. The polarization depends on time according to the expression

$$dP/dt = -P/\tau_{rec} + J \quad (2.4)$$

where τ_{rec} is the recombination time between electrons and holes (τ_{rec} = 10 ps for LT-GaAs) and $J = env_h + (-e)nv_e$ is the current density. The far-field radiation is given by

$$E_{THz} \propto \partial J/\partial t \propto ev\partial n/\partial t + en\partial v/\partial t\ , \quad (2.5)$$

where $v = v_e - v_h$. The transient electromagnetic field E_{THz} consists of two terms: the first term describes the carrier density charge effect while the second term describes the effect of charge acceleration due to the electric field bias.

2.1.2 Generation of THz Radiation Using Electro-Optic Materials

An alternative method [11] to generate THz radiation is using EO materials illuminated with fs laser pulses. When laser pulses normally incident on a thin EO slab of thickness L, the far-field field *E* generated by this rectified polarization can be obtained by solving the wave equation:

$$\frac{\partial^2 E}{\partial x^2} - \frac{\varepsilon_s}{c^2}\frac{\partial^2 E}{\partial t^2} = \frac{\partial^2 P^{NL}}{\partial t^2} \tag{2.6}$$

assuming that (i) the laser spot size is large enough to use plan wave approximation and the laser pulse propagates in the *x* direction; (ii) the rectification dipole P^{NL} is perpendicular to *x*; (iii) using the static dielectric constant of the media, ε_s, the dispersion of the radiation field is ignored. The solution of Eq. (2.6) at the region *x* >L can be found:

$$E(x,t) = \frac{\frac{c}{\upsilon_s}+\frac{c}{\upsilon}}{1+\frac{c}{\upsilon_s}} P^{NL}\left(t-\frac{x-L}{c}-\frac{L}{\upsilon}\right) - \frac{2\frac{c}{\upsilon_s}\left(1+\frac{c}{\upsilon}\right)}{\left(1+\frac{c}{\upsilon_s}\right)^2} P^{NL}\left(t-\frac{x-L}{c}-\frac{L}{\upsilon_s}\right) \tag{2.7}$$

where *c*, *v*, and v_s are the speed of the laser beam in the air, in the medium, and the speed of radiation beam in the medium, respectively.

2.1.3 Detection of THz Radiation Using PC Antennas

The electric field of a Gaussian beam on the detector [12] as shown in Fig. 2.1 can be expressed as:

$$E(x,y) = E_0 \exp[-(x^2+y^2)/w_1^2] \tag{2.8}$$

where w_1 is spot size. The total resistance over the detector is:

$$R = \frac{\rho_M L_M + \rho_M L_S}{td} \approx \frac{\rho_S L_S}{td} \tag{2.9}$$

where L_M is the total length of the metal electrodes, L_S is the length of the switch area between the two electrode tips, ρ_M and ρ_S are their resistivities, respectively, and d is the width of the electrode and the gap area. The average resistivity ρ_S is much larger than ρ_M owing to the low duty cycle of the driving laser (100 fs/10 ns =10^{-5}). The resistivity ρ_S depends on the photogenerated carrier density, which for homogeneous illumination of power P_{laser} scales as

$$\rho_S = \frac{L_S d}{\xi P_{laser}} \tag{2.10}$$

where ξ is a conversion factor between laser power and number of photogenerated carriers. The average field strength $\overline{E}$ across the detector gives rise to a potential difference $U = \overline{E}(L_M + L_S)$, so the average current is

$$I = \frac{U}{R} = \frac{\overline{E}(L_M + L_S)}{L_S^2} td\xi P_{laser} \tag{2.11}$$

The average electric field across the detector area is

$$\begin{aligned} \overline{E(L,d)} &= \frac{1}{Ld}\int_{-L/2}^{L/2}\int_{-d/2}^{d/2} E(x,y)dxdy \\ &= \frac{E_0 \pi w_1^2}{Ld} Erf\left(\frac{L}{2w_1}\right) Erf\left(\frac{d}{2w_1}\right) \end{aligned} \tag{2.22}$$

where *Erf* is the error function, and $L = L_M + L_S$. The peak strength of the electric field, E_0, can be expressed in terms of the total power in the THz beam:

$$P_{THz} = \frac{1}{2} c\varepsilon_0 \int_{-\infty}^{\infty}\int_{-\infty}^{\infty} E^2(x,y)dxdy = \frac{1}{2}\pi w_1^2 c\varepsilon_0 E_0^2 \tag{2.13}$$

$$\Rightarrow E_0 = \frac{2}{w_1}\sqrt{\frac{P_{THz}}{\pi c \varepsilon_0}} \tag{2.14}$$

By inserting Eq. (2.14) into the expression for the detector current, Eq. (2.11), we get

$$I(\upsilon) = \xi P_{laser}\sqrt{\frac{cP_{THz}}{\pi\varepsilon_0}}\frac{2R_L t}{L_S^2 d\omega_0 (n-1)}\frac{1}{\upsilon}Erf[\frac{L}{2}\frac{(n-1)\pi w_0}{cR_L}\upsilon]Erf[\frac{d}{2}\frac{(n-1)\pi w_0}{cR_L}\upsilon] \tag{2.15}$$

when focusing spot size $\lim_{\lambda\to 0} w_1(d_{focus}) = \frac{c}{\pi\upsilon\omega_0}\frac{R_L}{(n-1)}$.

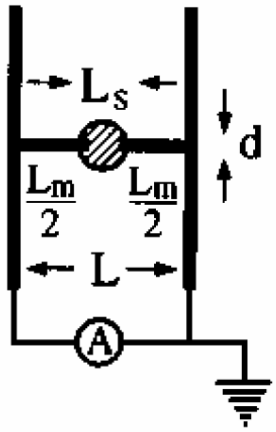

Fig. 2.1 Structure of antenna detector

2.1.4 Detection of THz Radiation Using EO Materials

Detection of the polarization change of an optical probe beam produced by the THz field when both fields are applied on an electro-optic crystal; this method is called free-space-electro-optic sampling (FS-EOS).

The FS-EOS uses the linear electro-optic effect in an EO crystal excited by an optical probe field and the THz field. Both fields propagate in the same direction but have different polarizations. For instance, if *z* is the propagation direction, the optical probe is polarized at 45° in the (*x*, *y*)

plane perpendicular to *z* owing to birefringence of the EO crystal, while the THz field is perpendicular to the y axis. Since the electro-optic effect is practically instantaneous at the THz scale, the output of a FS-EOS detector is directly proportional to $E_{\mathrm{THz}}(t)$. Due to the presence of the THz field a phase retardation $\Delta\varphi$ of the optical field is produced over the distance dz, which is strongly dependent on the electro-optic crystal type and orientation. ZnTe is a material for which a high signal-to-noise ratio is obtained. For ZnTe the phase retardation is given by

$$\Delta\varphi(\tau) = (\omega / c) n_0^3 r_{41} E_{THz}(\tau) dz = const_{ZnTe} \times E_{THz}(\tau) dz \qquad (2.16)$$

where ω is the optical frequency of the probe and r_{41} is the electro-optic coefficient. From the above equation it follows that the THz field can be obtained after propagating over a length L in a ZnTe crystal, a material with small absorption and a refractive index difference of $\Delta n = n_{\mathrm{THz}} - n_{\mathrm{opt}} = 0.22$, is

$$E_{THz}(\tau) = \Delta\varphi(\tau) / (L \times const_{ZnTe}) . \qquad (2.17)$$

Thus, measuring the phase change we can determine the time variation of the THz signal $E_{\mathrm{THz}}(t)$.

2.1.5 Applications

THz technologies have made great progress for aiming at applications such as radio astronomy, remote-sensing, spectroscopy [13-15], optical properties of semiconductors and dielectrics [16], imaging of general substances [17-19], and biomedical imaging [20-21]. It also can be applied to find specific spectroscopic fingerprints of biological matter in this region [22].

2.2 Metallic Photonic Crystals

Photonic crystals are periodically structured electromagnetic media, generally possessing photonic band gaps: ranges of frequency in which light cannot propagate through the structure. The crystal can thus form a kind of perfect optical "insulator," which can confine light losslessly around sharp bands, in lower-index media, and within wavelength-scale cavities, and among other novel possibilities for control of electromagnetic phenomena.

2.2.1 Metallic Photonic Crystals

Photonic crystals made of metals are called "Metallic Photonic Crystals" (MPCs) which have been widely used to form bandpass filters, reflector surfaces, Fabry-Perot interferometers, and so forth.

2.2.1.1 Infinite-long Circular waveguides

Fig. 2.2 shows electromagnetic (em) waves can propagate inside round metal pipes with radius of a. Equations of time-harmonic electric and magnetic field can be written as following:

$$\nabla^2 E + k^2 E = 0$$
$$\nabla^2 H + k^2 H = 0 \qquad (2.18)$$

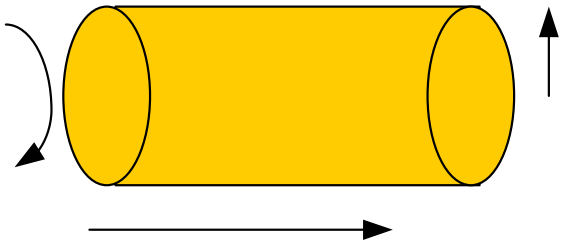

Fig. 2.2 A circular waveguides

For a straight and uniform circular waveguide, as shown in Fig. 2.2, it is convenient to decompose the 3-D Laplacian operator ∇^2 into two parts: $\nabla_{r\phi}^2$ and ∇_z^2 for transverse and longitudinal components, respectively. For TM waves, $H_z = 0$ and $E_z \neq 0$, all fields can be expressed in terms of $E_z = E_z^0 e^{-\gamma z}$, where E_z^0 satisfies the homogeneous Helmholtz's equation

$$\begin{aligned} &\nabla_{r\phi}^2 E_z^0 + (\gamma^2 + k^2) E_z^0 = 0 \\ &or \quad \nabla_{r\phi}^2 E_z^0 + h^2 E_z^0 = 0 \end{aligned} \quad . \tag{2.19}$$

For TE waves, $E_z = 0$ and $H_z \neq 0$, all fields can be expressed in terms of $H_z = H_z^0 e^{-\gamma z}$, where H_z^0 satisfies the same homogeneous Helmholtz's equation listed above.

For TM waves in circular waveguides,

$$E_z(r,\phi,z) = E_z^0(r,\phi)e^{-\gamma z} . \tag{2.20}$$

The solutions are

$$\begin{aligned} E_z^0 &= C_n J_n(hr)\cos n\phi \\ E_r^0 &= -\frac{j\beta}{h} C_n J_n'(hr)\cos n\phi \\ E_\phi^0 &= -\frac{j\beta n}{h^2 r} C_n J_n(hr)\sin n\phi \\ H_r^0 &= -\frac{j\omega\varepsilon n}{h^2 r} C_n J_n(hr)\sin n\phi \\ H_\phi^0 &= -\frac{j\omega\varepsilon}{h} C_n J_n'(hr)\cos n\phi \\ H_z^0 &= 0 \end{aligned} \tag{2.21}$$

where $j\beta$ is equal to γ, J_n is a Bessel function, and C_n is a coefficient. The eigenvalues of TM modes are determined from the boundary condition that E_z^0 must vanish at r = a:

$$J_n(ha) = 0 \tag{2.22}$$

For the lowest TM mode, TM_{01},

$$(h)_{TM_{01}} = \frac{2.405}{a}, \tag{2.23}$$

which yields the lowest cutoff frequency:

$$(f_c)_{TM_{01}} = \frac{(h)_{TM_{01}}}{2\pi\sqrt{\mu\varepsilon}} = \frac{0.383}{a\sqrt{\mu\varepsilon}} \quad \text{(Hz)} \tag{2.24}$$

For TE waves in circular waveguides,

$$H_z(r,\phi,z) = H_z^0(r,\phi)e^{-\gamma z} \tag{2.25}$$

The solutions are

$$\begin{aligned}
H_z^0 &= C_n' J_n(hr)\cos n\phi \\
H_r^0 &= -\frac{j\beta}{h} C_n' J_n'(hr)\cos n\phi \\
H_\phi^0 &= \frac{j\beta n}{h^2 r} C_n' J_n(hr)\sin n\phi \\
E_r^0 &= \frac{j\omega\mu n}{h^2 r} C_n' J_n(hr)\sin n\phi \\
E_\phi^0 &= \frac{j\omega\mu}{h} C_n' J_n'(hr)\cos n\phi \\
E_z^0 &= 0
\end{aligned} \tag{2.26}$$

where C_n' is a coefficient. The eigenvalues of TE modes are determined from the boundary condition that the normal derivative of H_z^0 must vanish at r = a:

$$J_n'(ha) = 0 \tag{2.27}$$

For the lowest TE mode, TE_{11},

$$(h)_{TE_{11}} = \frac{1.841}{a}, \tag{2.28}$$

which yields the lowest cutoff frequency:

$$(f_c)_{TE_{11}} = \frac{(h)_{TE_{01}}}{2\pi\sqrt{\mu\varepsilon}} = \frac{0.293}{a\sqrt{\mu\varepsilon}} \quad \text{(Hz)} \tag{2.29}$$

2.2.1.2 Chen's theory

In this thesis a robust theory [23] based on microwave circuit problems to calculate transmission spectra of our MPCs was used. The theory in detail is shown below:

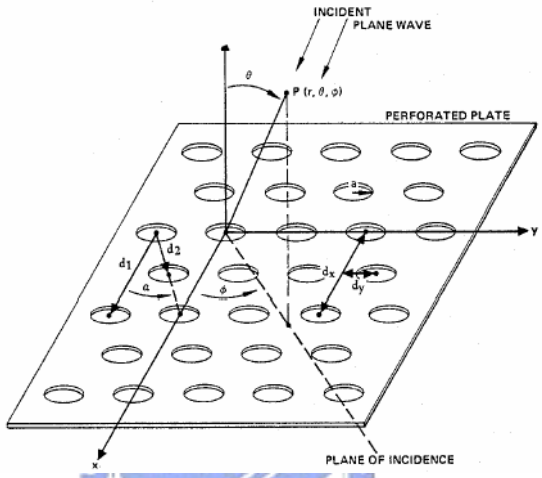

Fig. 2.3 Geometry of a perforated plate

The fields on both sides of the plate as shown in Fig. 2.3 are expanded into a complete set of Floquet modes Φ_{pqr}, with two spatial harmonic number p and q, and a third subscript r, used to denoted TE or TM mode. Each Floquet mode has a propagation constant γ_{pq} along the z axis and a characteristic modal wave admittance ξ_{prq}^{f}. The fields inside the holes between two apertures are expressed in terms of conventional waveguide modes Ψ_{mn} with a characteristic modal wave admittance η_{mn} and a propagation constant β_{mn}. The incident wave is of arbitrary polarization with modal voltage coefficient A_{001} and A_{002}. By matching the transverse electric and magnetic fields at the aperture $z = -l_1$, an integral equation for the unknown transverse field at $z = -l_1$ is obtained:

$$2\sum_{r=1}^{2} A_{00r}\xi_{00r}^{f}\Phi_{00r} = \sum_{r=1}^{2}\sum_{p}^{\infty}\sum_{q}^{\infty}\xi_{pqr}^{f}\Phi_{pqr}\iint_{aperture}\Phi_{pqr}^{*}\cdot E_t\,da + \sum_{r=1}^{2}\sum_{p}^{\infty}\sum_{q}^{\infty}F_{mnr}Y_{mnr}\Psi_{mnr}$$

(2.30)

p, q = 0, ±1, ±2,….., ±∞

m, n = 0, 1, 2,….., ∞

where F_{mnr} and Y_{mnr} are the modal coefficient of the conventional waveguide modes and the input admittance looking into the waveguide from the aperture at $z = -l_1$, respectively. In the cases of open and short circuits at $z = 0$, the input admittance is

$$Y_{mnr} = +j\eta_{mnr}\tan(\beta_{mnr}l_1) \qquad \text{for open circuit}$$

$$= -j\eta_{mnr}\cot(\beta_{mnr}l_1) \qquad \text{for short circuit} \qquad (2.31)$$

By substituting (2.31) into (2.30), two integral equations, one for the open-circuit and the other for the short-circuit problem, are obtained. The open- and short-circuit aperture fields at $z = -l_1$, $\boldsymbol{E_o}$ and $\boldsymbol{E_s}$ are obtained by solving these two integral equations independently by the method of moments. Thus the transverse aperture fields at $z = -l_1$ of the original problem are

$$E_t(z = \mp l_1) = \frac{1}{2}[E_o \pm E_s] \qquad (2.32)$$

where the positive sign applies to the aperture field on the incident side of the plate, and the negative sign applies to the aperture field on the transmitted side. The reflection coefficient at $z = -l_1$ is

$$R_{pqr} = \iint_{aperture} E_t(z = -l_1)\Phi_{pqr}^{*}\,da - \delta_{pq}A_{00r} \qquad (2.33)$$

where $\delta_{pq}=1$ for $p = q = 0$, otherwise $\delta_{pq}=0$.

The transmission coefficient at $z = l_1$ is

$$B_{pqr} = \iint_{aperture} E_t(z = l_1) \cdot \Phi^*_{pqr} da \tag{2.34}$$

For the case of normal incidence, the reflection and the transmission coefficients are reduced to the forms

$$R = \frac{1}{1 - j[A + B\tanh(\beta l)} + \frac{1}{1 - j[A + B\coth(\beta l)]} - 1 \tag{2.35}$$

$$T = \frac{1}{1 - j[A + B\tanh(\beta l)} - \frac{1}{1 - j[A + B\coth(\beta l)]} \tag{2.36}$$

where A and B are functions of element spacing and aperture size. For circular openings with equilateral triangular lattice:

$$A = 12(\frac{4}{3}(\frac{\lambda}{d})^2 - 1)^{1/2}[\frac{J_1'(\frac{4\pi}{\sqrt{3}}\frac{a}{d})}{1 - (\frac{4\pi a}{1.841\sqrt{3}d})^2}]^2 - \frac{12}{(\frac{4}{3}(\frac{\lambda}{d})^2 - 1)^{1/2}}[\frac{J_1(\frac{4\pi}{\sqrt{3}}\frac{a}{d})}{\frac{4\pi}{\sqrt{3}}\frac{a}{d}}]^2 \tag{2.37}$$

for $a > 0.28\ d$ and $d < 0.57\ \lambda$

$$B = 0.33(\frac{d}{a})^2((\frac{0.293\lambda}{a})^2 - 1)^{1/2} \tag{2.38}$$

$$\beta = \frac{2\pi}{\lambda}((\frac{0.293\lambda}{a})^2 - 1)^{1/2} \tag{2.39}$$

where a is the radius of circular apertures and d is the spacing between any two apertures.

2.2.1.3 Theory of Surface Plasmons (SPs) [24]

The electron charges on a metal boundary can perform coherent fluctuations that are called surface plasma oscillations [25]. The field of surface plasma on smooth surface, Fig. 2.4, can be expressed as

$$E = E_0^{\pm} \exp[+i(k_x x \pm k_z z - wt)] \tag{2.40}$$

where $k_x = 2\pi / \lambda_p$. According to boundary conditions,

$$D_0 = \frac{k_{z1}}{\varepsilon_1} + \frac{k_{z2}}{\varepsilon_2} = 0 \tag{2.41}$$

$$\varepsilon_i (\frac{w}{c})^2 = k_x^2 + k_{zi}^2 \tag{2.42}$$

The dispersion relation (2.42) can be written as

$$\Rightarrow k_x = \frac{w}{c} (\frac{\varepsilon_1 \varepsilon_2}{\varepsilon_1 + \varepsilon_2})^{1/2}, \tag{2.43}$$

shown in Fig. 2.5. Besides a real ω and ε_2, assuming that $\varepsilon_1'' < |\varepsilon_1'|$,

$$\begin{aligned} k_x^{'} &= \frac{w}{c} (\frac{\varepsilon_1^{'} \varepsilon_2}{\varepsilon_1^{'} + \varepsilon_2})^{1/2} \\ k_x^{''} &= \frac{w}{c} (\frac{\varepsilon_1^{'} \varepsilon_2}{\varepsilon_1^{'} + \varepsilon_2})^{3/2} \frac{\varepsilon_1^{''}}{2(\varepsilon_1^{'})^2} \end{aligned} \tag{2.44}$$

when $\begin{aligned} \varepsilon_1 &= \varepsilon_1^{'} + i\varepsilon_1^{''} \\ \varepsilon_2 &= \varepsilon_2^{'} + i\varepsilon_2^{''} \\ k_x &= k_x^{'} + ik_x^{''} \end{aligned}$ can be obtained.

For metal and semiconductor $\varepsilon_1^{'} < 0$ and $|\varepsilon_1^{'}| > \varepsilon_2$, k_x' is real.

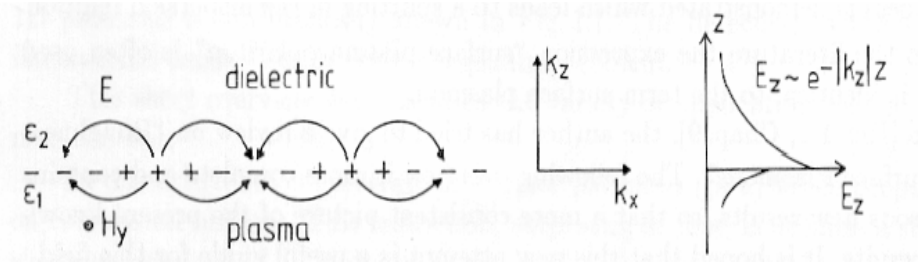

Fig.2.4 The charges and the em field of SPs propagating on a surface in the x direction.

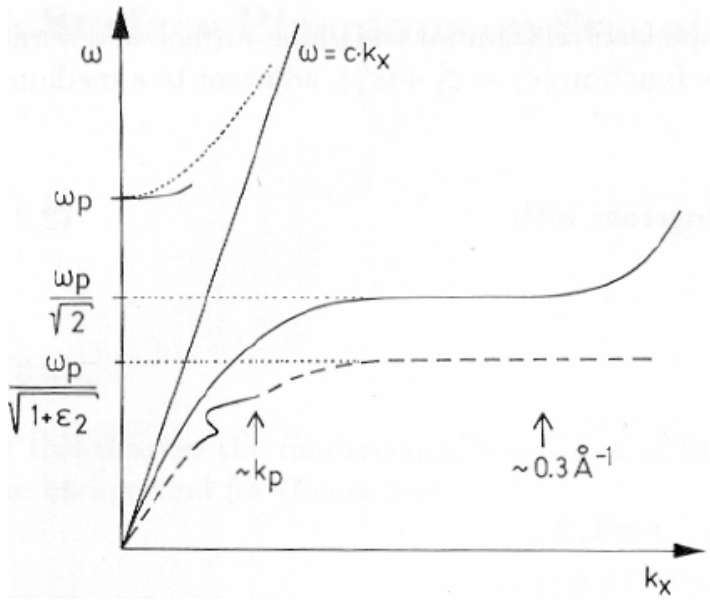

Fig. 2.5 The dispersion relation of SPs and light in vacuum

From the results of Fig. 2.5, it indicates that SPs cannot transform into light without any assistance. Grating components are used to couple the light to SPs as depicted in Fig. 2.6. Light wave vector is increased by a $\Delta k_X = \upsilon\, g$ (υ: integer) value to "transform" the photons into SPs.

$$k_x = \frac{w}{c}\sin\theta_0 \pm \nu g = \frac{w}{c}\sqrt{\frac{\varepsilon_m \varepsilon_d}{\varepsilon_m + \varepsilon_d}} = k_{sp} \qquad (2.45)$$

The reverse also takes place: SPs propagate along the grating to reduce K_X by ΔK_X. Then SPs is transformed into Light.

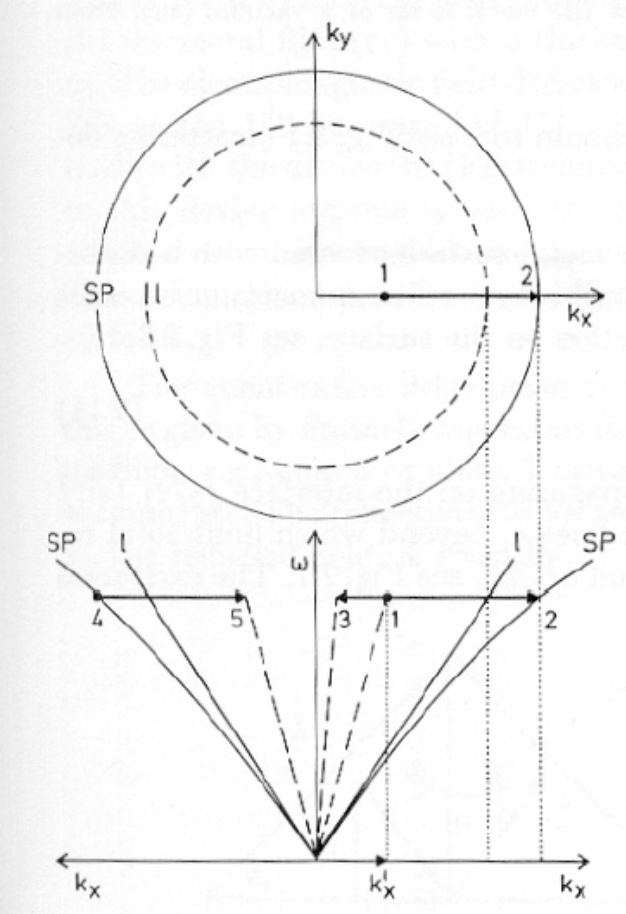

Fig. 2.6 The grating coupler. SP: dispersion relation of SPs, *l*: light line

For a 2-D rectangular grating [26], and tilted incident light with wave vector $\vec{k}$,

$$\vec{k}_{sp} = \vec{k}_x + i\vec{G}_x + j\vec{G}_y = \vec{k}\sin\theta + i\frac{2\pi}{a}\hat{x} + j\frac{2\pi}{b}\hat{y} \qquad (2.46)$$

where $\vec{G}_x$ and $\vec{G}_y$ are reciprocal lattice vectors, i and j are integers, a and b are holes periodicities along the principal axes, and θ is incident angle. In the case of a square lattice with periodicity of a_0, together with Eq. (2.45), the dispersion relation of SPs is given by

$$\left|k_{sp}\right| = [(\frac{2\pi}{\lambda}\sin\theta + i\frac{2\pi}{a_0})^2 + (j\frac{2\pi}{a_0})^2]^{1/2} = \frac{\omega}{c}(\frac{\varepsilon_d\varepsilon_m}{\varepsilon_d+\varepsilon_m})^{1/2} \quad (2.47)$$

For a triangular lattice of holes, however, Eq. (2.47) gives the position of the maxima if normal incidence:

$$\lambda_{\max} = a_0[\frac{4}{3}(i^2+ij+j^2)]^{-1/2}(\frac{\varepsilon_d\varepsilon_m}{\varepsilon_d+\varepsilon_m})^{1/2}. \quad (2.48)$$

In THz region, ε_m is a much larger value than ε_d so the

$$\lambda_{\max} \propto \varepsilon_d^{1/2} \quad (2.49)$$

2.2.2 Transmission Characteristics of MPCs

From this theory, transmission properties of MPCs are independent on the polarization of normal incident waves. Recently, Miyamaru et al. [3] showed that no polarization change was observed because two orthogonal-polarized electric fields along the principal axes of the triangular lattice after passing through the MPC had equal transmittance and phase shifts.

3. Experimental Methods

3.1 THz-TDS System

The THz-TDS system was shown in the Fig. 3.1(a), and transient current was generated optoelectronically by femtosecond laser pulses (1) impinging on a photoconducting material, dipole antenna on a GaAs:As^+ substrate (2). Emission of electromagnetic (em) pulses (3), THz radiation, of about ps duration were produced by the current. The THz pulse was collected and guided by gold-coated parabolic mirrors (4). Fs laser pulse as a probe beam with time delayed by motor stage (6) and the THz pulse collinearly impinged on a nonlinear crystal (ZnTe) (8). The transmitted laser pulse with polarization changed by electro-optical effect was separated into two beams with orthogonal polarizations by Wollaston beam splitter (9). The two beams coupled to a balanced detector (10) connecting to a lock-in amplifier (LIA) (11). Signal from LIA can be easily obtained using PC.

To reduce the water vapor absorption of THz signal, an acrylic box by continuously introducing pure nitrogen was used as a humidity controller in THz optics. The humidity can be rapidly lowered to few percents in tens of minutes. Furthermore, due to the stable atmosphere in THz optics, the THz system became more stable.

Assuming that the THz beam was spatial Gaussian distribution, the THz radiation can be considered as a plane wave, i.e. normal incident to the sample when the sample was located in the image plane, as shown in Fig. 3.1 (b).Consequently, the analysis was simplified to normal transmission.

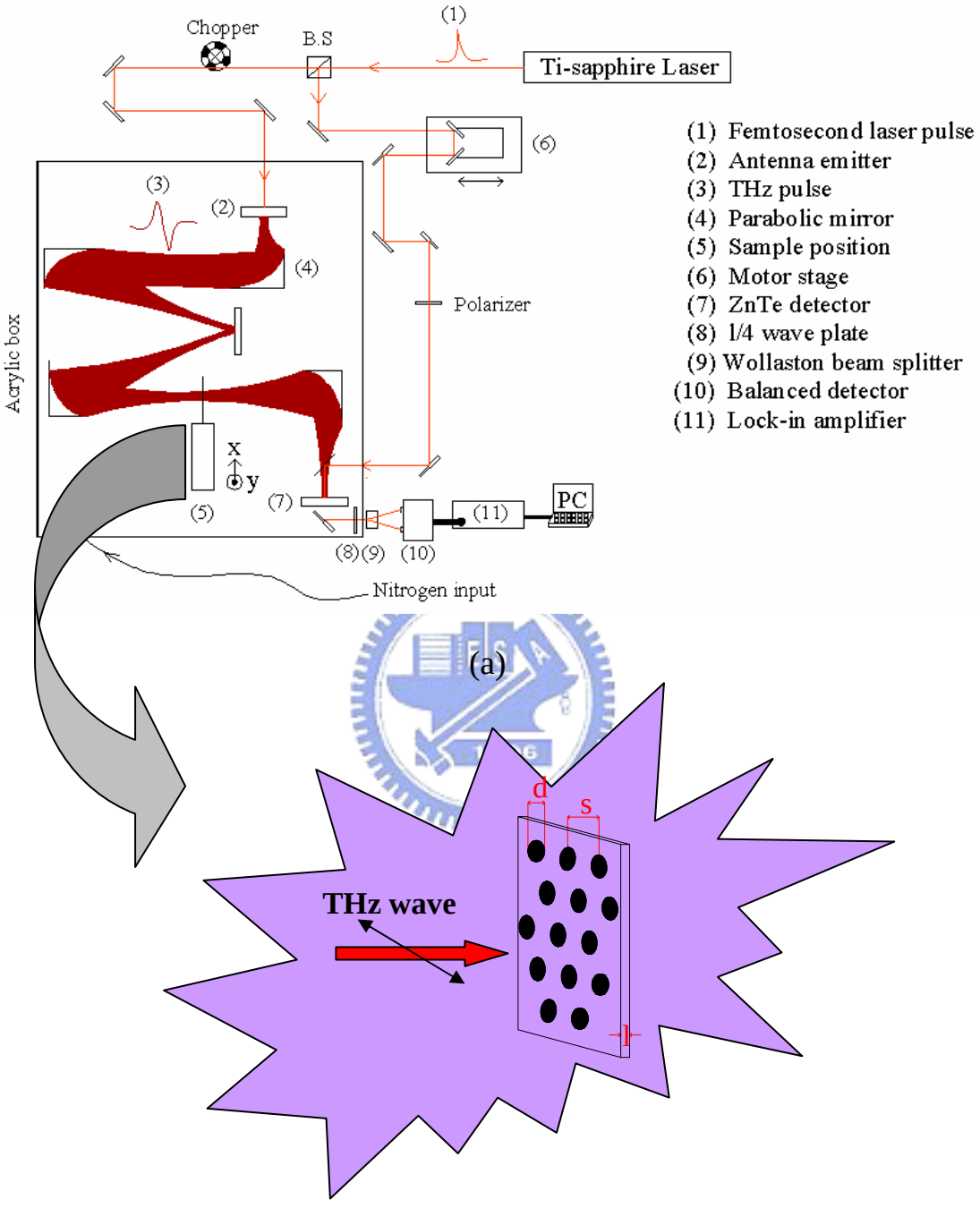

Fig. 3.1 THz-TDS system

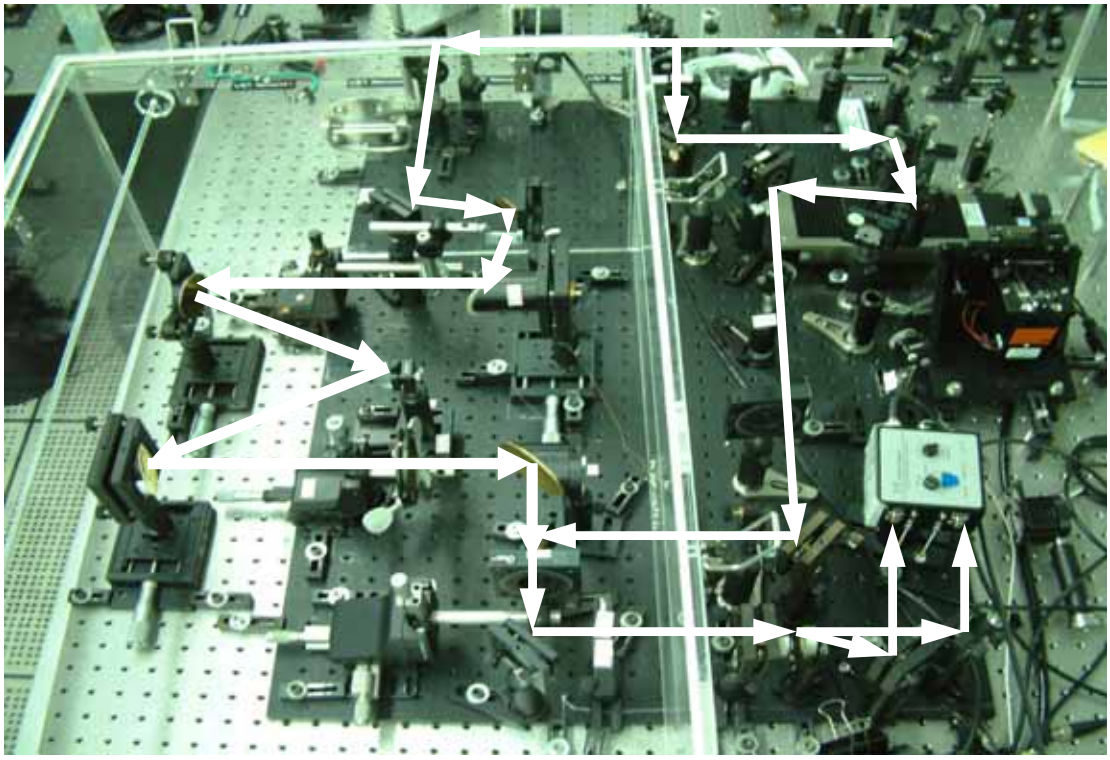

(a)

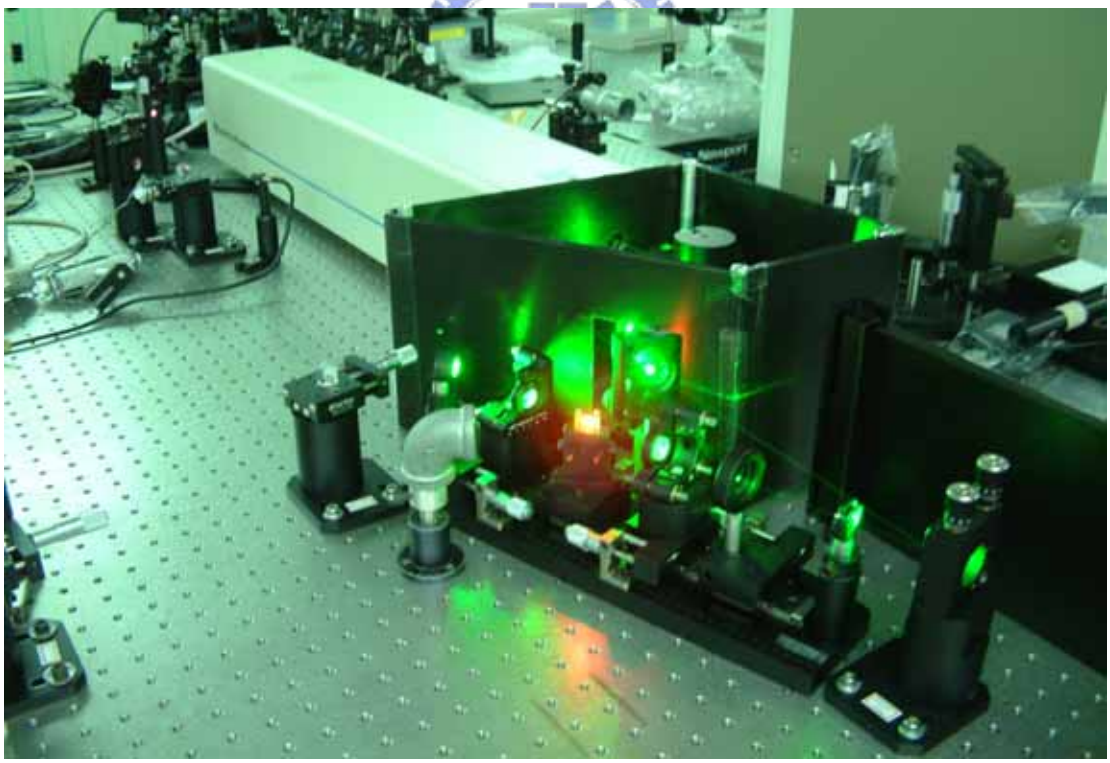

(b)

Fig. 3.2 Real pictures of (a) THz-TDS system and (b) Ti-sapphire ultrafast laser

3.2 Fabrication methods

One of fabrication methods for MPCs is to use laser cutting by a high-power pulsed laser. Laser cutting provided high-speed, precise orientation to form vector, raster cutting and etching capabilities over a range of materials. Its mechanism was shown in Fig. 3.3. Another method is mechanical manufacture. It also provides sufficiently fine structures to meet our need.

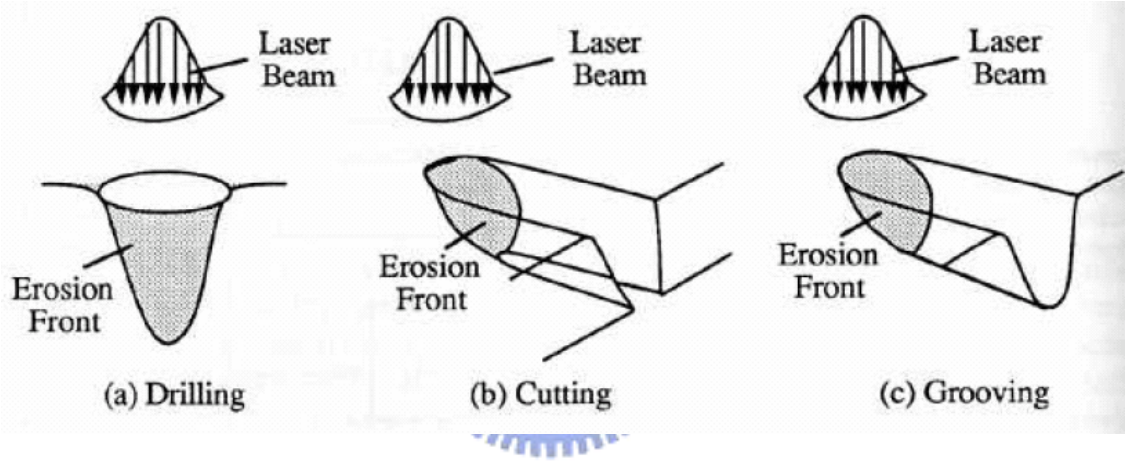

Fig. 3.3 Laser cutting mechanism (from MIT Media Lab)

3.3 Structures of MPCs Samples

All samples were metal slabs perforated periodically with a triangular array of circular holes. Three parameters (s: spacing between holes, d: diameter of holes, l: slab thickness) can be controlled to change the transmission properties of MPCs. One of samples named JMPC is made of aluminum alloy and produced by mechanical manufacture in Japan. The others named #1 to #3 are made of stainless steels SUS-304 and produced by laser cutting by La Kang Co., LTD.

3.4 Sampling and Data Processing

Transmission properties were noteworthy issue in MPCs. Using THz-TDS method, amplitude information can be easily obtained. First, resolution in frequency-domain corresponding to the empirical data sheet, shown in Appendix 1, was chosen.

Second, THz radiation propagating through W/O a MPC as a MPC signal or a reference, respectively, was measured. Two time-domain waveforms can be used to obtain frequency-domain spectra using numerical fast Fourier transform, and then the MPC data divided by the reference should be the amplitude transmittance of this sample. Power transmittance was the square of the amplitude transmittance. The transmission properties of a certain sample at different frequencies can be observed.

4. Experimental results and discussion

4.1 Free Space THz-TDS Waveforms and Spectra

When THz radiation propagates through optical component in the same distance but with different humidity, THz time-domain waveforms are shown in Fig. 4.1. The amplitude of oscillations after main peaks decreasing as the humidity decreases can be found. It can speculate that the oscillation is caused by water vapor absorption. From the Fig. 4.1 (d), the noise is lowered after N_2 purged. Moreover, the signal to noise ratio (S/N ratio) is better after vapor exhausted. Fig. 4.2 depicted the spectra with 0.0073 THz resolution of fast Fourier Transform of these waveforms. Some deep dips at 0.556, 0.754, 0.988, 1.113, 1.164, 1.208, 1.230, 1.413 THz disappear as the humidity goes down. This is obviously due to absorption of water vapor, which are consistent with the results of van Exter et al. [27].

Besides, in the insect of Fig. 4.2, regular oscillations, high frequency fringes, are found in spectrum. When other antennas of different kinds, i.e. different refractive index, or thickness of substrate are used, the oscillation frequency is changed. It is obvious that the major factor comes from the etalon effect between radiation and the substrate of the emitter. Appendix 2 shows the results in detail.

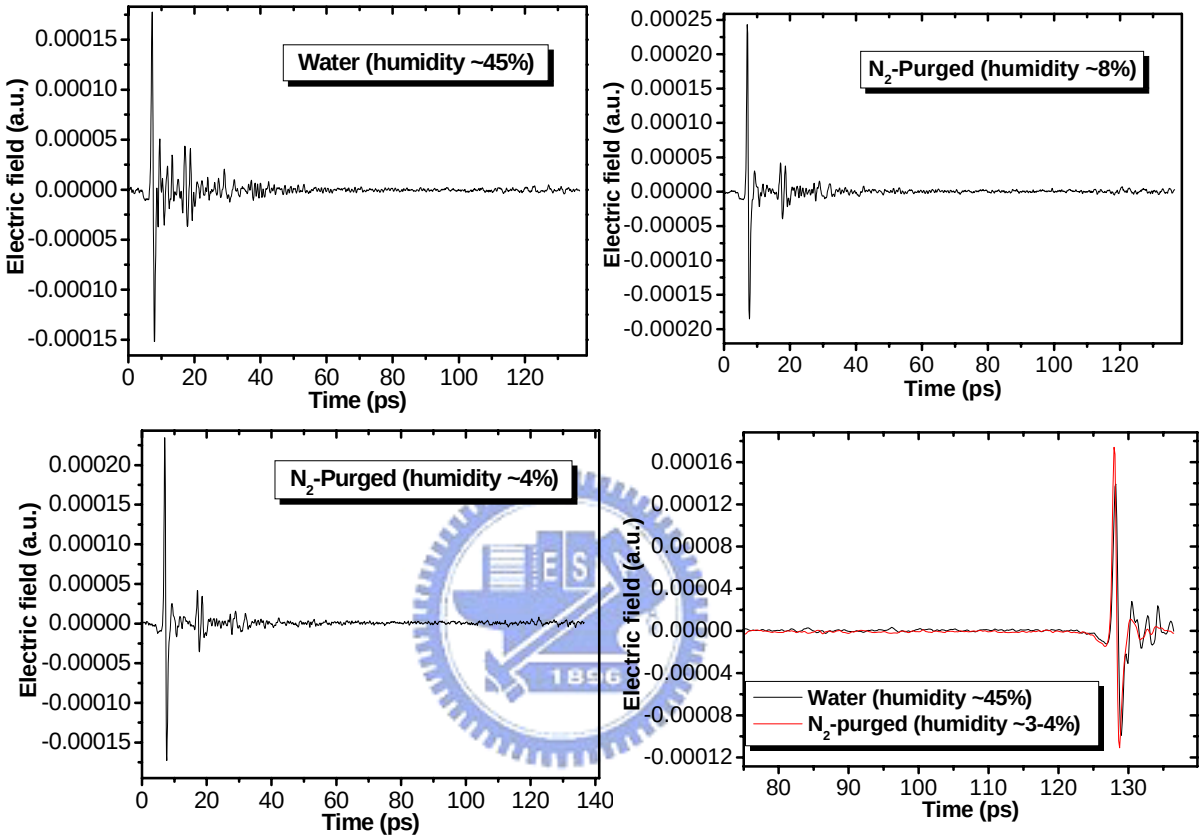

Fig. 4.1 Free space waveforms with humidity control

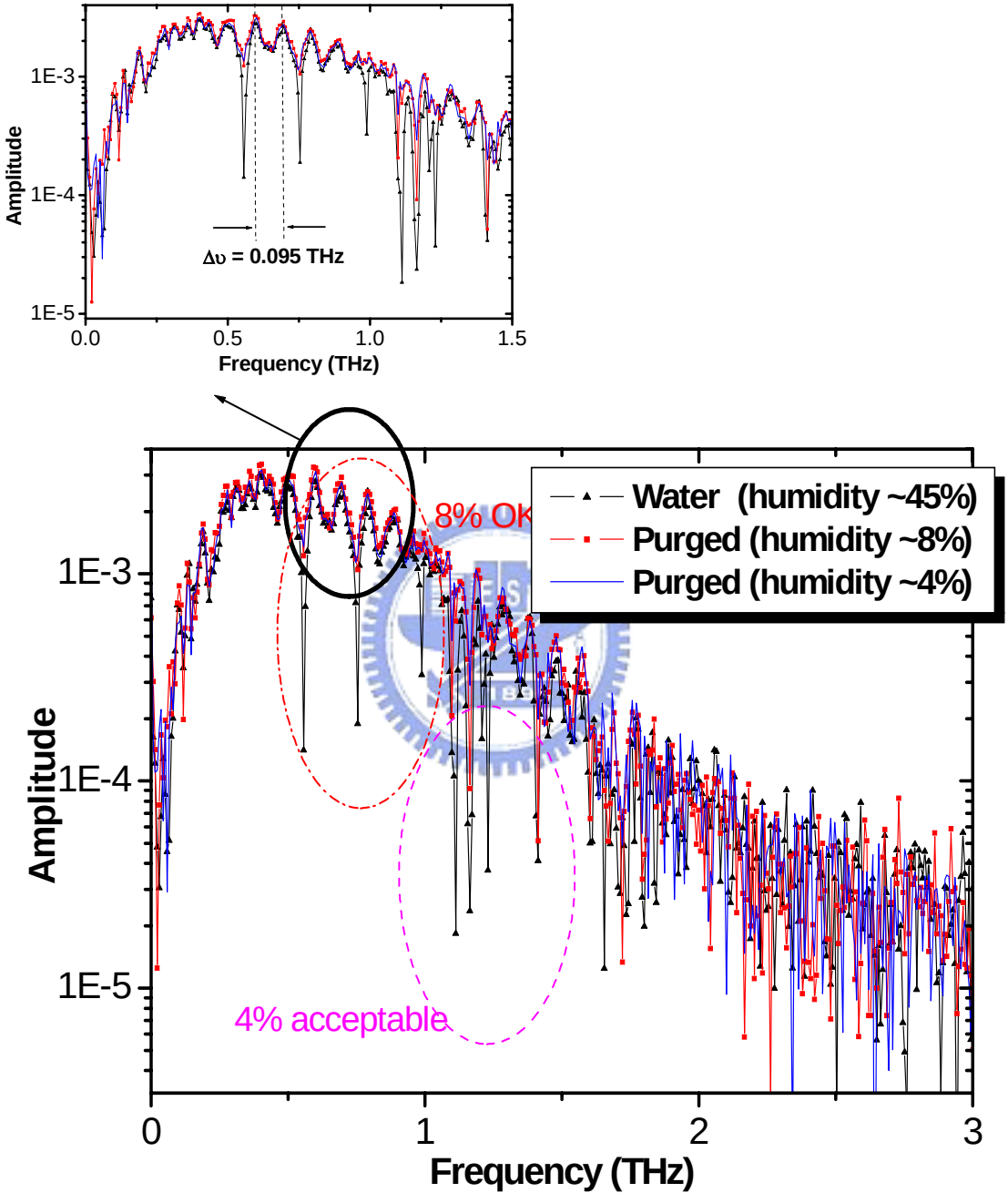

Fig. 4.2 FFT spectra of waveforms in Fig. 4.1

In June 26, 2004, a fire accident occurred in the basement of Engineering Building V which our laboratory is located in. This accident causes the change of free-space spectra as shown in Fig. 4.3. A significant change is found at 0.131 THz, where a deep dip caused by characteristic absorption line of sulfur dioxide [28]. It is obvious that sulfur dioxide is produced after fire accident and it can be found using THz-TDS technique.

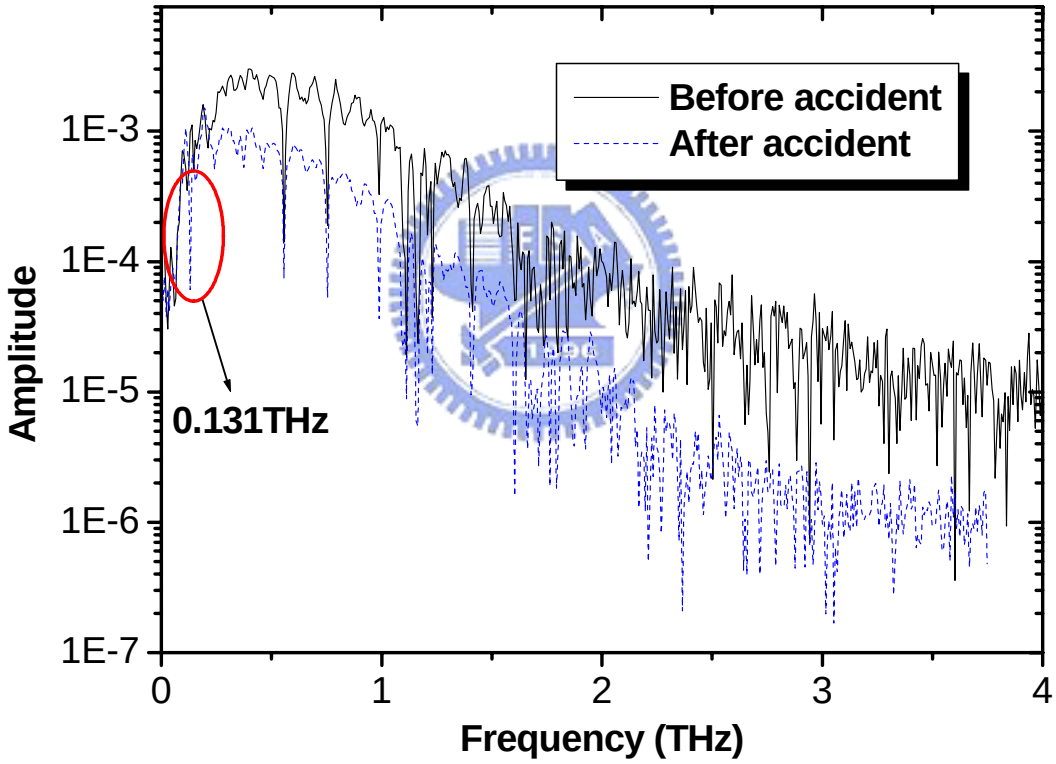

Fig. 4.3 Spectra comparison before and after fire accident

4.2 Metallic Photonic Crystals (MPCs)

4.2.1 Basic transmission properties of MPCs

Fig. 4.4 displayed pictures of four samples from a camera and an optical microscope. S, D, and L represent hole spacing, hole diameter, and plate thickness in unit of micron, respectively.

Individual THz waveforms and spectra of MPC samples were shown in Fig. 4.5 ~ 4.8. Each spectrum had clear forbidden band and almost unity transmittance at predicted frequency. Amplitude transmittance spectra ware depicted in Fig. 4.9. Obviously, it was hard to eliminate water vapor absorbed highly at 1.164, 1.669, 1.720 THz even though the low humidity ~5%. Some narrow and steep peaks were found due to too small signal at the specific frequencies by water vapor absorption.

In Fig. 4.10, it's clear that the experimental spectra of power transmittance were excellently coincidental with calculated spectra by Chen's theory. Among them, transmission spectrum of JMPC had better signal to noise ratio because the peak of the THz signal was around the cutoff frequency of JMPC.

The parameters used to characterize their transmission properties were listed in Table 4.1. In Table 4.1, experimental cutoff frequencies agreed well with those calculated according to Chen's theory, but had a little difference from those corresponding to the infinite-long circular waveguide theory. However, cutoff frequencies were well inversely proportional to diameters of holes as shown in Fig. 4.11

(a) S= 995 D= 565 L= 480

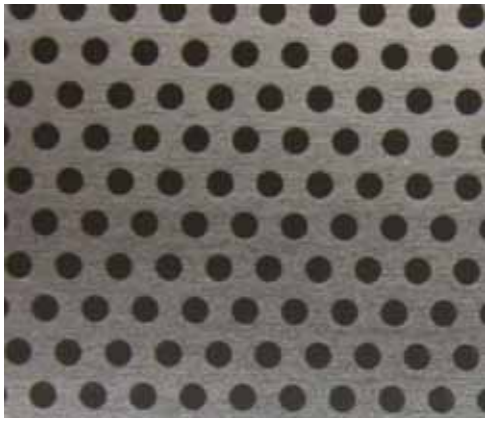

(b) S= 425 D= 284 L= 200

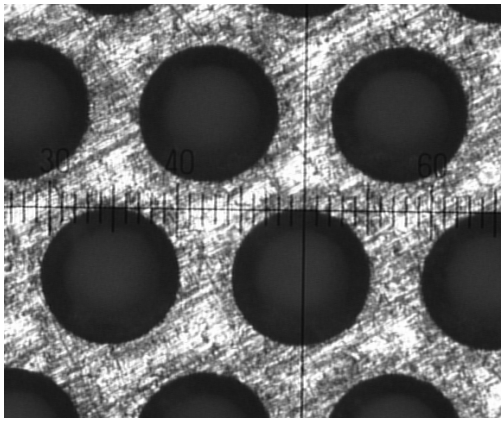

(c) S= 295 D= 248 L= 150

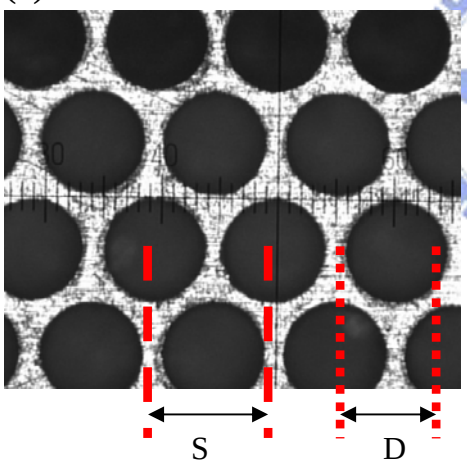

(d) S= 225 D= 155 L= 100

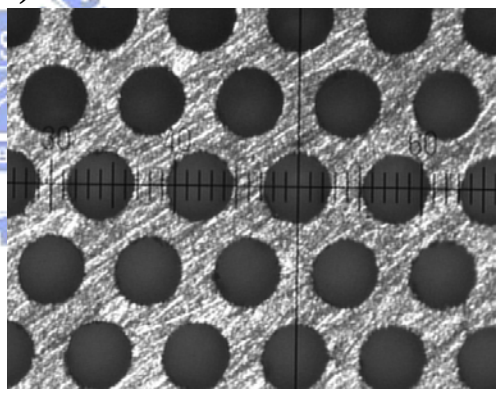

Fig. 4.4 Real pictures of (a) JMPC, (b) sample #1, (c) sample #2, and (d) sample #3. In unit of μm

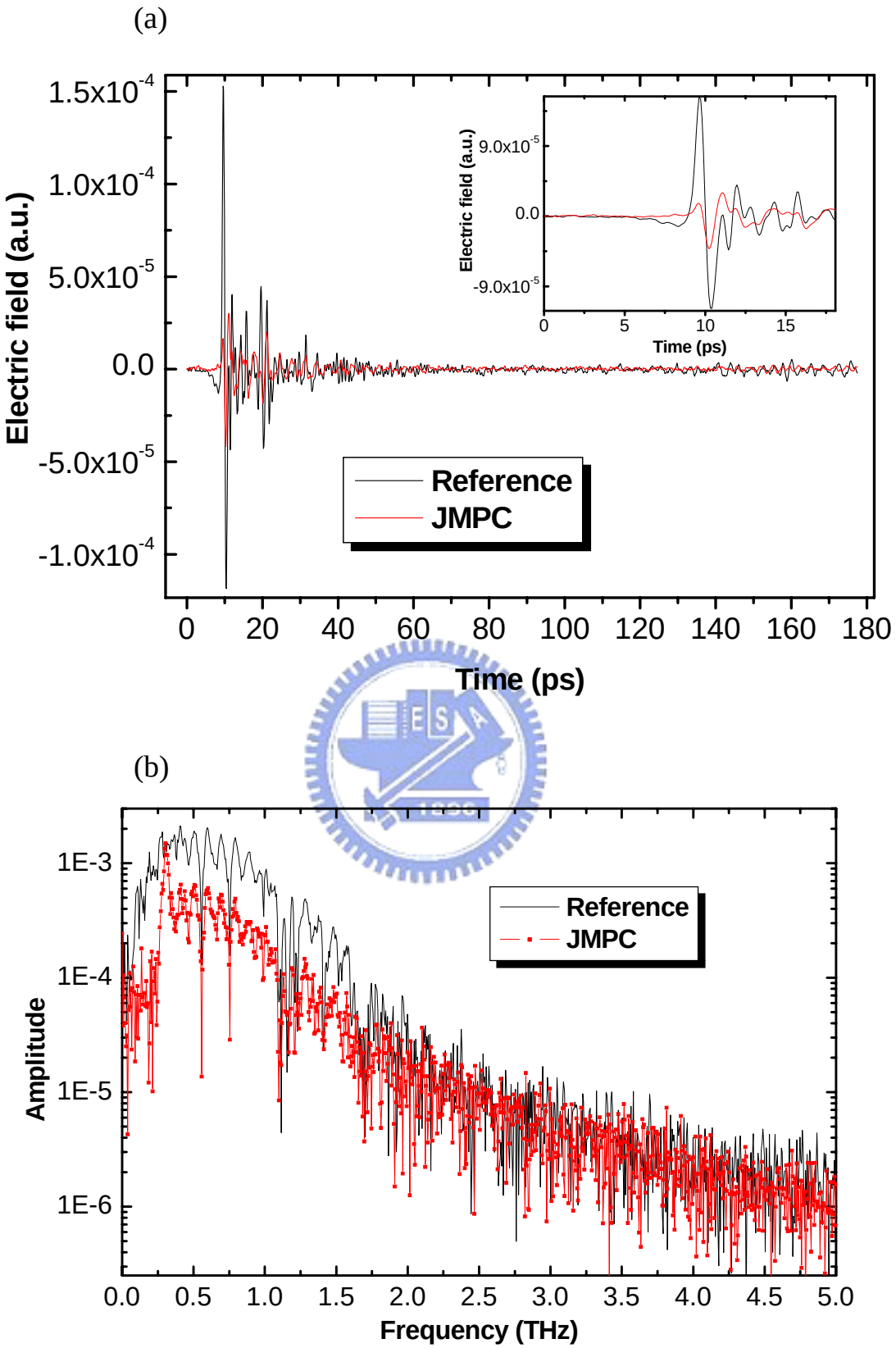

Fig. 4.5 (a) THz waveforms and (b) spectra of reference and JMPC

(a)

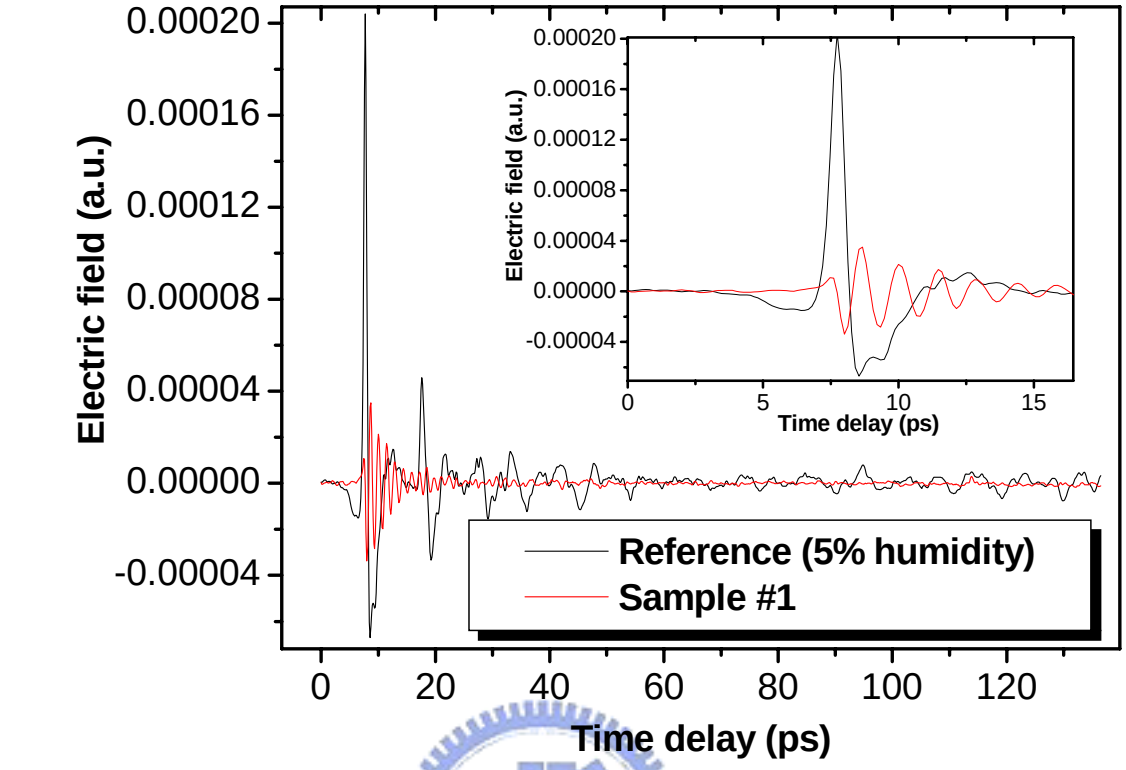

(b)

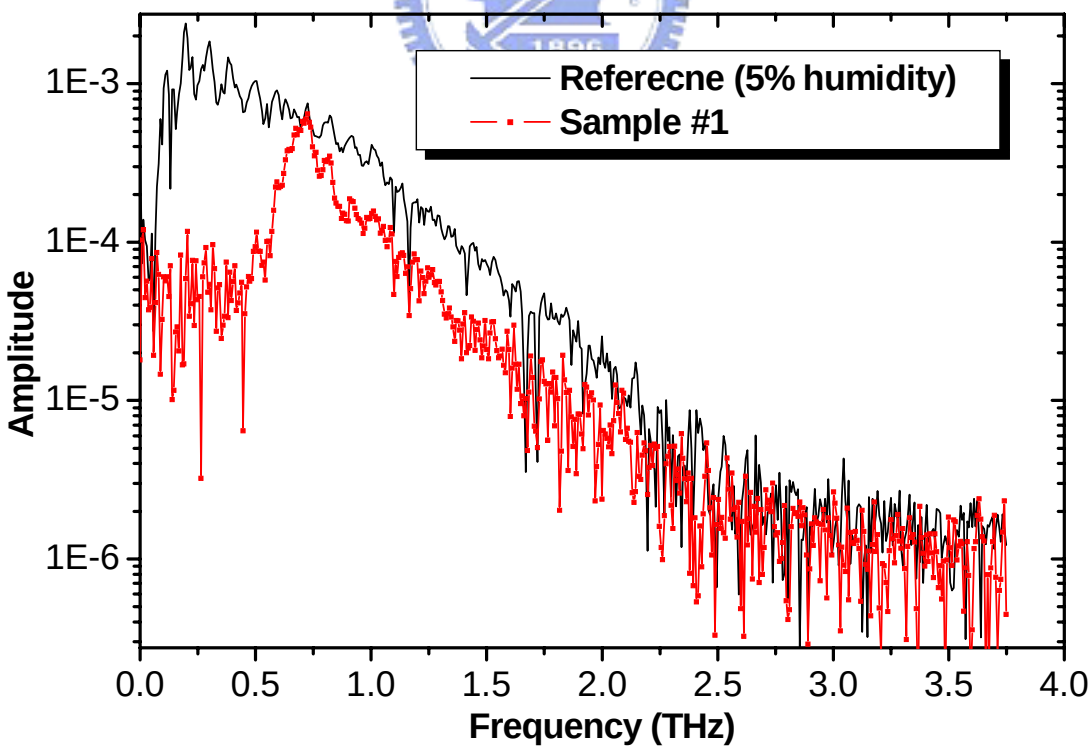

Fig. 4.6 (a) THz waveforms and (b) spectra of reference and sample #1

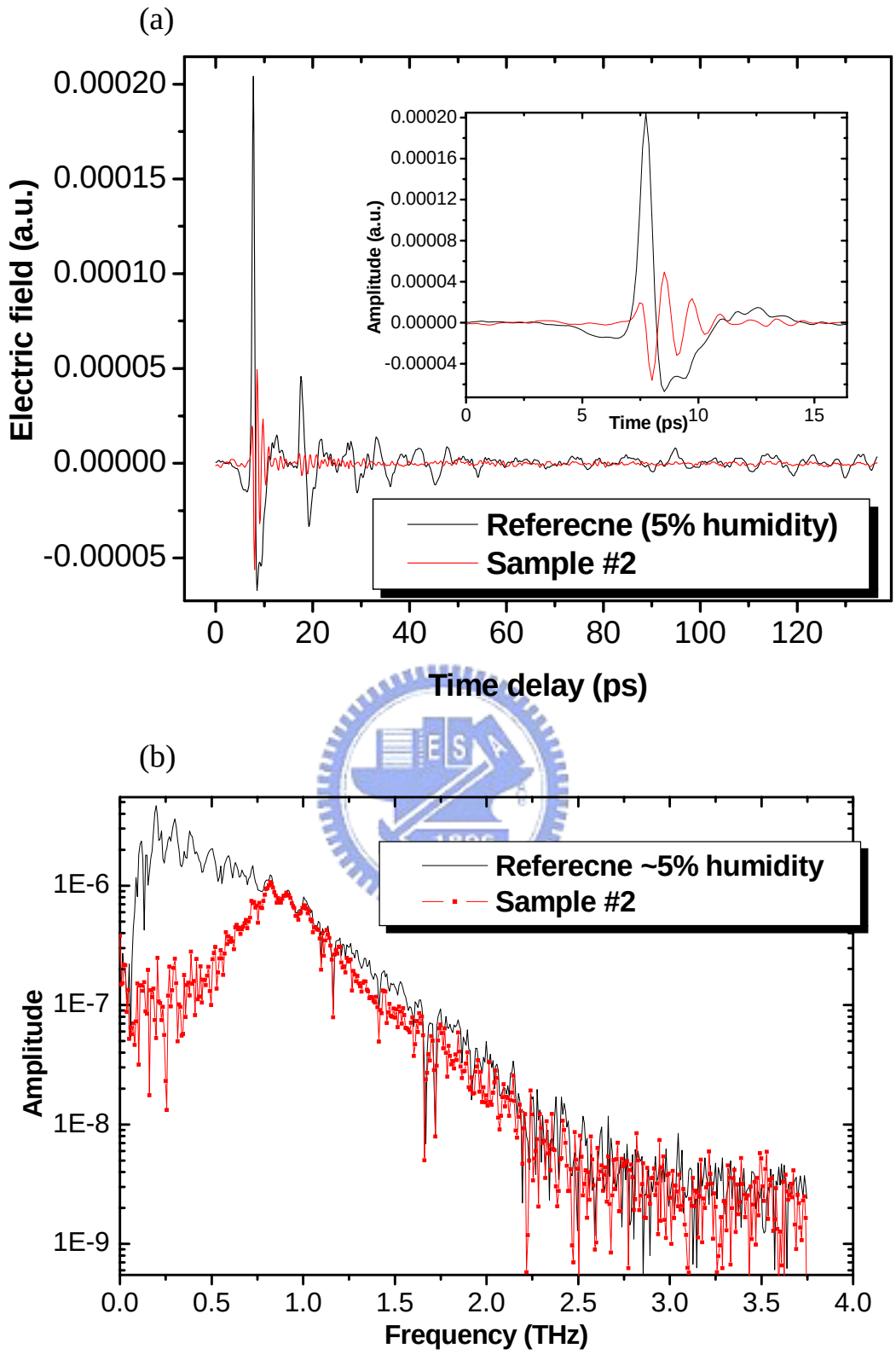

Fig. 4.7 (a) THz waveforms and (b) spectra of reference and sample #2

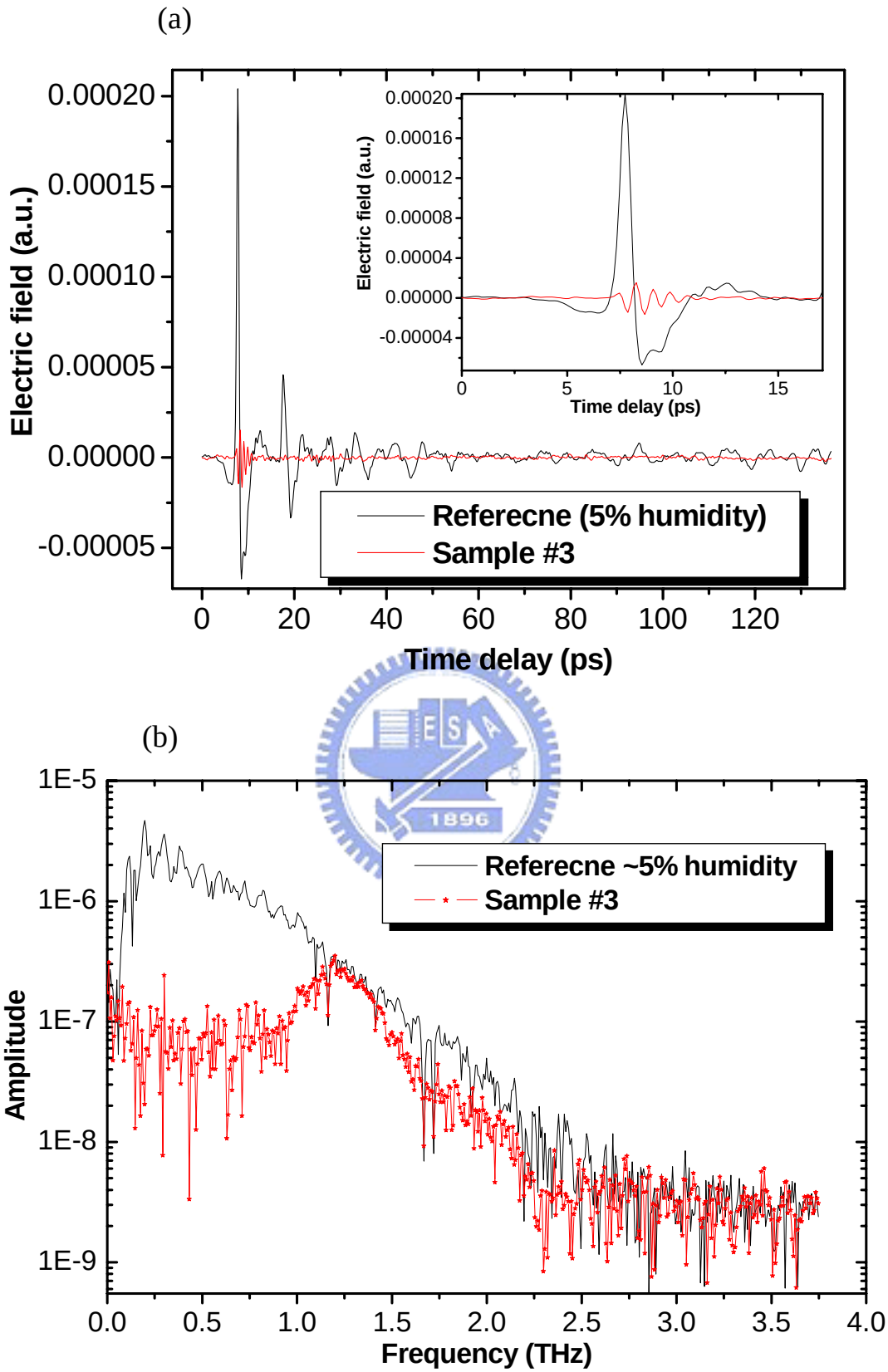

Fig. 4.8 (a) THz waveforms and (b) spectra of reference and sample #3

(a)

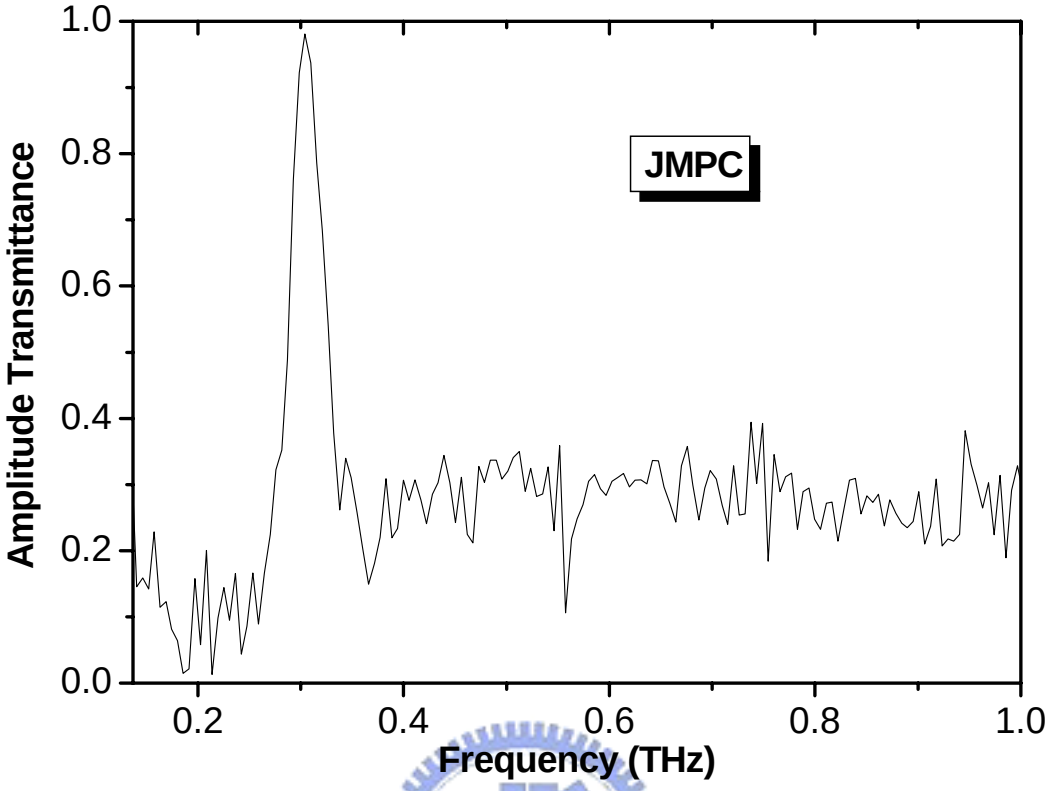
JMPC
Amplitude Transmittance
Frequency (THz)
1.0
0.8
0.6
0.4
0.2
0.0
0.2
0.4
0.6
0.8
1.0

(b)

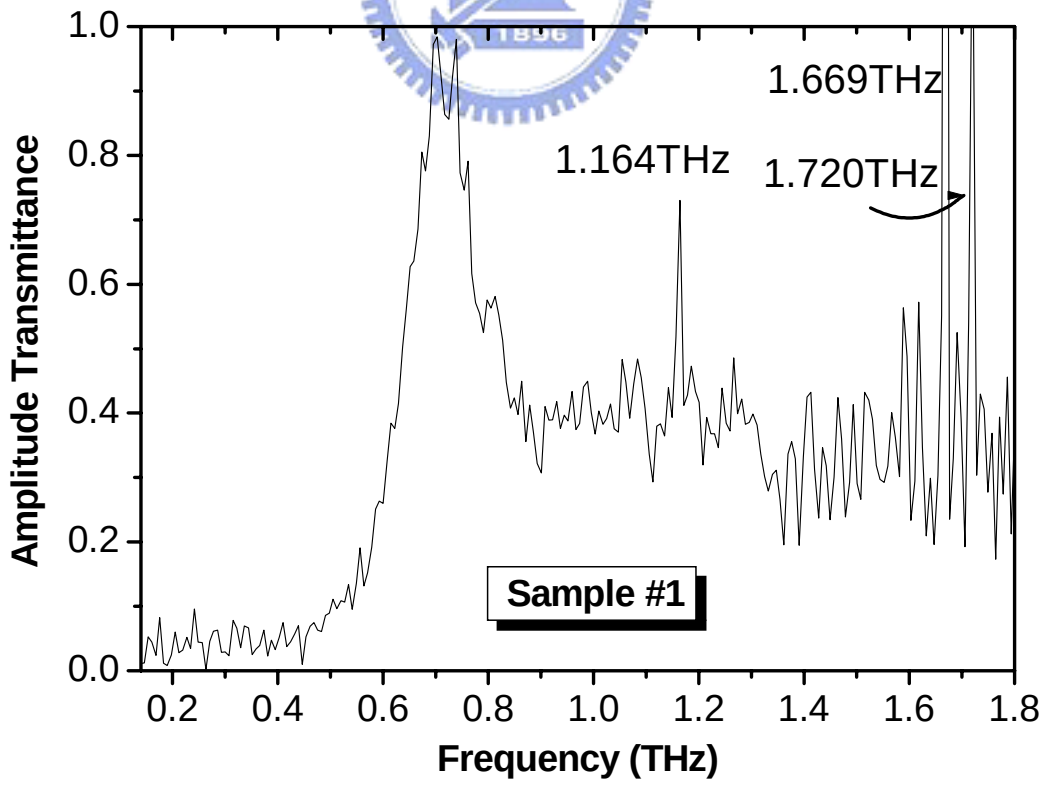
1.669THz
1.164THz
1.720THz
Sample #1
Amplitude Transmittance
Frequency (THz)
1.0
0.8
0.6
0.4
0.2
0.0
0.2
0.4
0.6
0.8
1.0
1.2
1.4
1.6
1.8

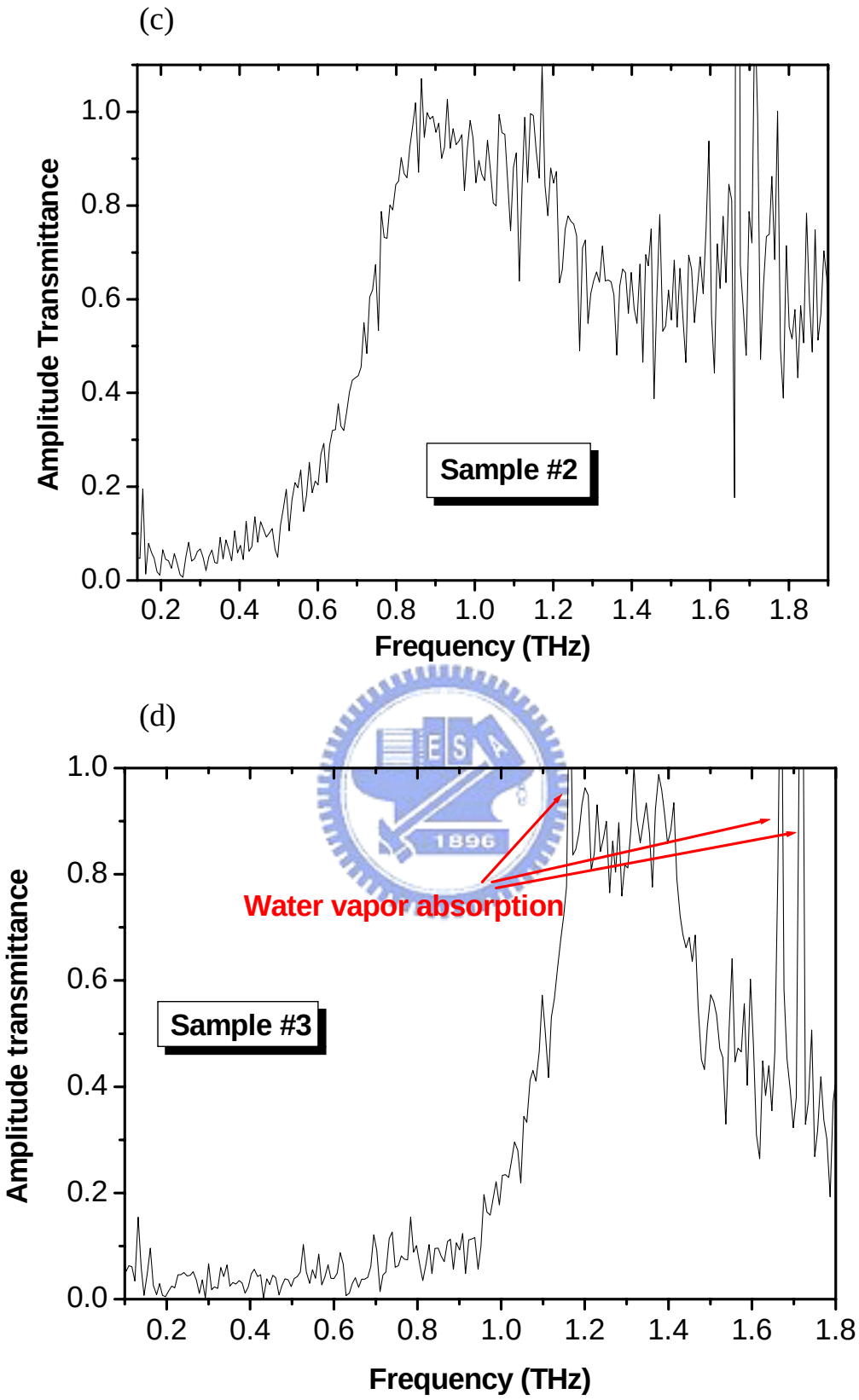

Fig. 4.9 Amplitude transmittance of (a) JMPC, (b) sample #1, (c) sample #2, and (d) sample #3

(a)

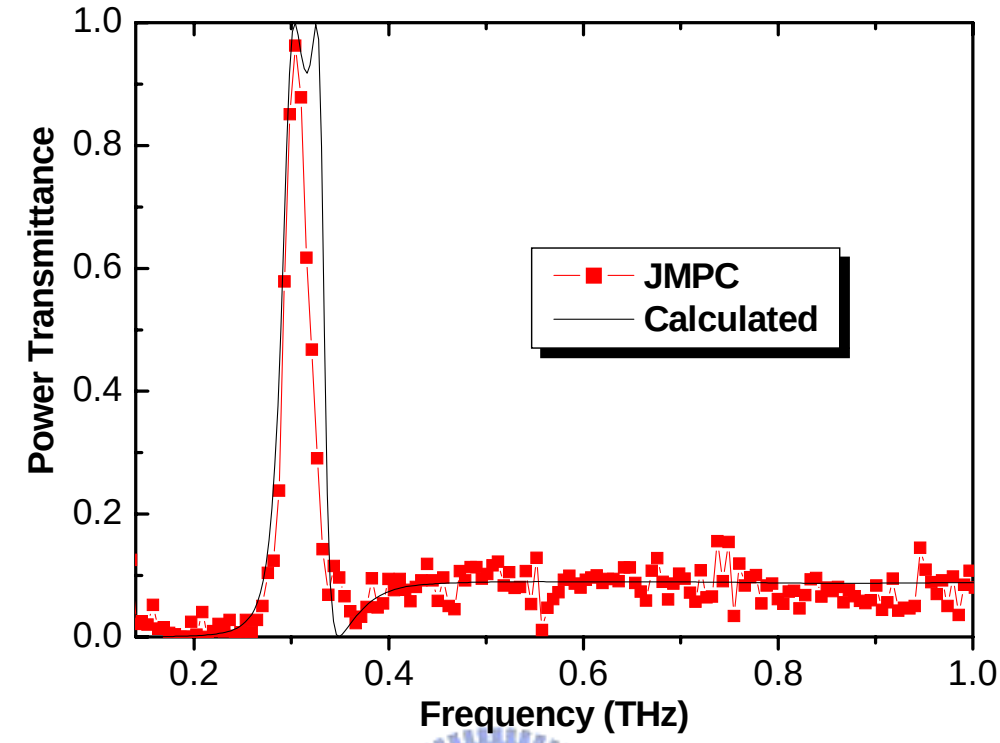
Power Transmittance
Frequency (THz)
JMPC
Calculated
1.0
0.8
0.6
0.4
0.2
0.0
0.2
0.4
0.6
0.8
1.0

(b)

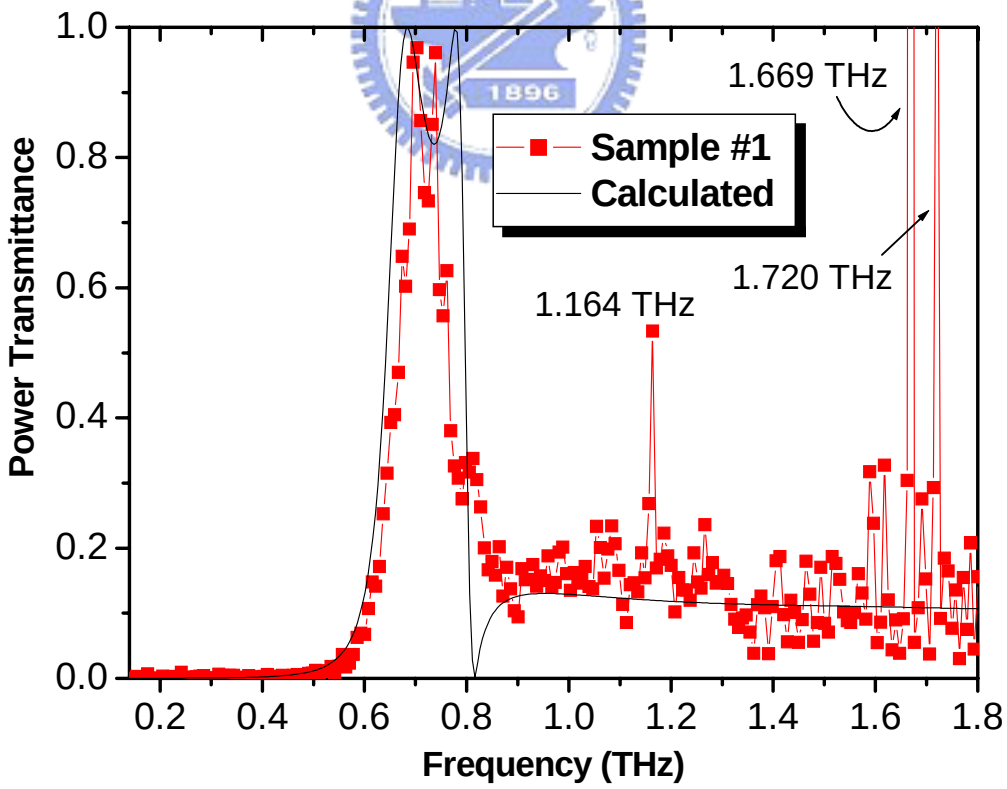
Power Transmittance
Frequency (THz)
Sample #1
Calculated
1.669 THz
1.720 THz
1.164 THz
1.0
0.8
0.6
0.4
0.2
0.0
0.2
0.4
0.6
0.8
1.0
1.2
1.4
1.6
1.8

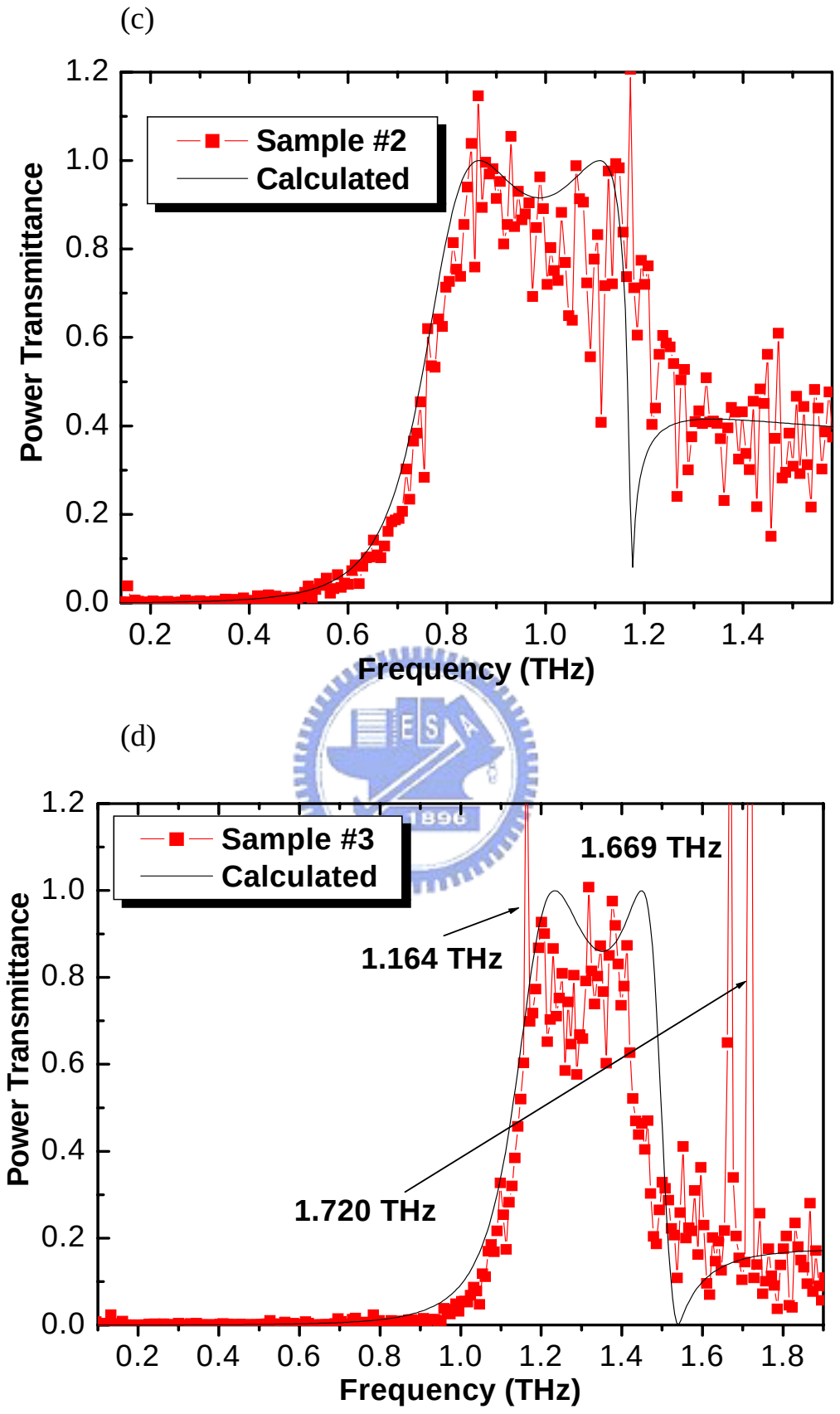

Fig. 4.10 Power transmittance of (a) JMPC, (b) sample #1, (c) sample #2, and (d) sample #3

Table 4.1 Parameters and characteristics of MPCs

Sample	S	D	L	υ_{cut}*	υ_{cut}^{c}	υ_{cut}^{exp}	$\upsilon_{diff}^{\$}$	$T_{porosity}$
JMPC	995	565	480	0.311	**0.289**	**0.289**	0.348	0.292
#1	425	284	200	0.619	**0.642**	**0.660**	0.815	0.405
#2	295	248	150	0.709	**0.746**	**0.754**	1.174	0.641
#3	225	155	100	1.134	**1.129**	**1.142**	1.539	0.430

S, D, L: in unit of μm.

υ_{cut}*,υ_{cut}^{c}, υ_{cut}^{exp} , $\upsilon_{diff}^{\#}$: in unit of THz

c: according to Chen's theory

*: infinite circular waveguide theory

$T_{porosity}$: the proportion of the hole area to the aperture area

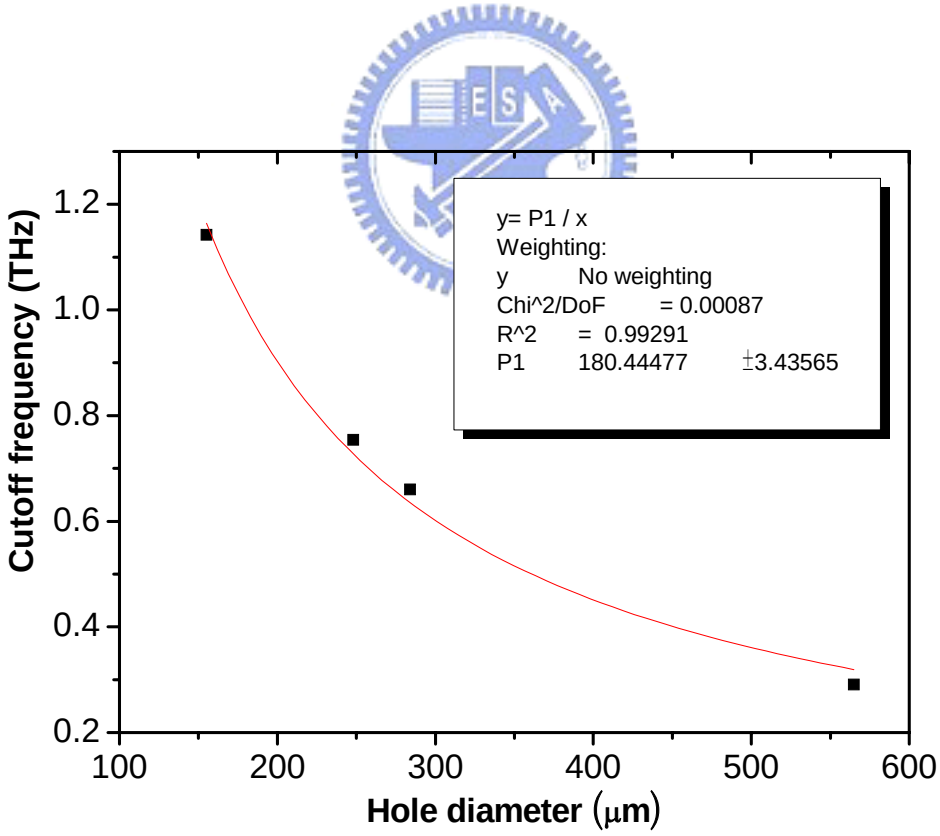

Fig. 4.11 Cutoff frequency vs. holes diameter of MPCs

4.2.2 Polarization rotated around the optical axis of sample #1

From the results of Fig. 4.12, it can be known that normal transmission of THz radiation with different polarizations is the same. The same results are also shown in Miyamaru et al. When the incident angle is zero, transmission is independent of the polarization due to equal phase difference and transmittance of two orthogonal polarizations.

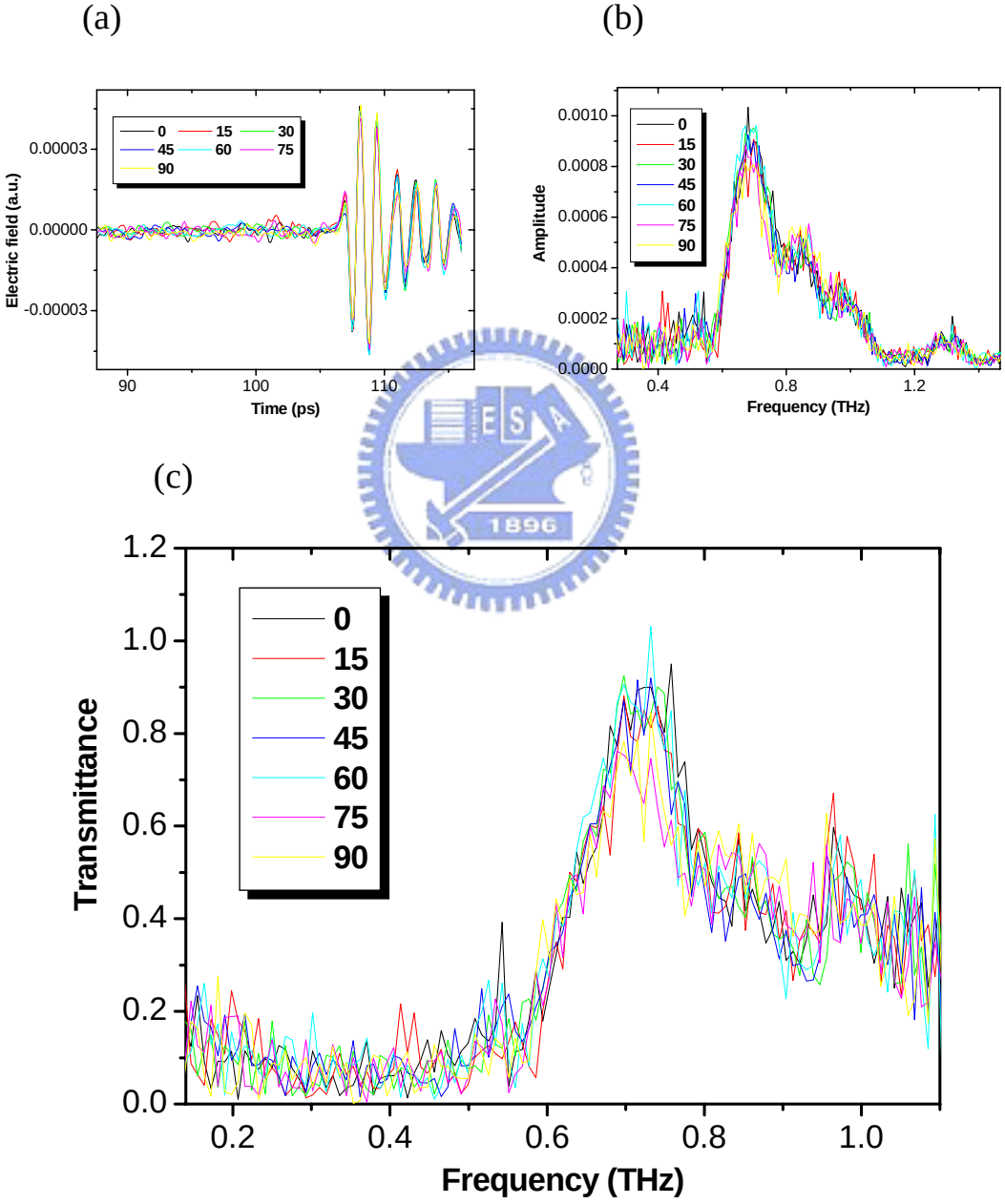

Fig. 4.12 (a) Waveforms, (b) spectra, and (c) transmittances of Sample #1 with rotation

4.2.3 Transmission properties of MPCs with 3M tapes

Fig. 4.13 shows that the spectra and the transmittance of 1 to 4 layers of 3M tapes of 60 μm thickness. In Fig. 4.13 (b), the tapes are almost transparent to THz radiation of 0.1 ~ 1 THz. If the tapes attached to the incident side of MPCs, Fig. 4.14 displays that transmission peaks shifted to low frequency and the peak amplitude dropped more than the attenuation effect of tapes in Fig. 4.13.

It is showed transmittance spectra of JMPC without tapes, with one tape on incident side, and with one tape on each side in Fig. 4.15. The magnitude of transmission peak dropped to ~60% and the peak frequency shifts from 0.309 THz to 0.282 THz as one tape is attached to the incident side of JMPC. If another tape is attached to the other side of JMPC, the magnitude of transmission peak rises to almost equal transmittance of JMPC without tapes, and the peak frequency shifts again to lower frequency ~ 0.266 THz. The change of peak frequency may be caused by the surface plasma effect. The transmittance of JMPC with one tape on each side is larger than that of JMPC with one tape on incident side, which is attributed to impedance matching on both interfaces of input and output sides.

Fig. 4.16 shows that shifts of peak frequencies are obviously observed. Transmittance at peak frequency monotonically decayed until the saturation when number of tapes is four. Moreover, peak frequencies shift to lower frequencies below cutoff. Shifting to lower frequency is related to surface plasma effect.

From Fig. 4.15 and 4.17, it could be deduced that tapes attached to each side of JMPC should produce larger transmittance

(a)

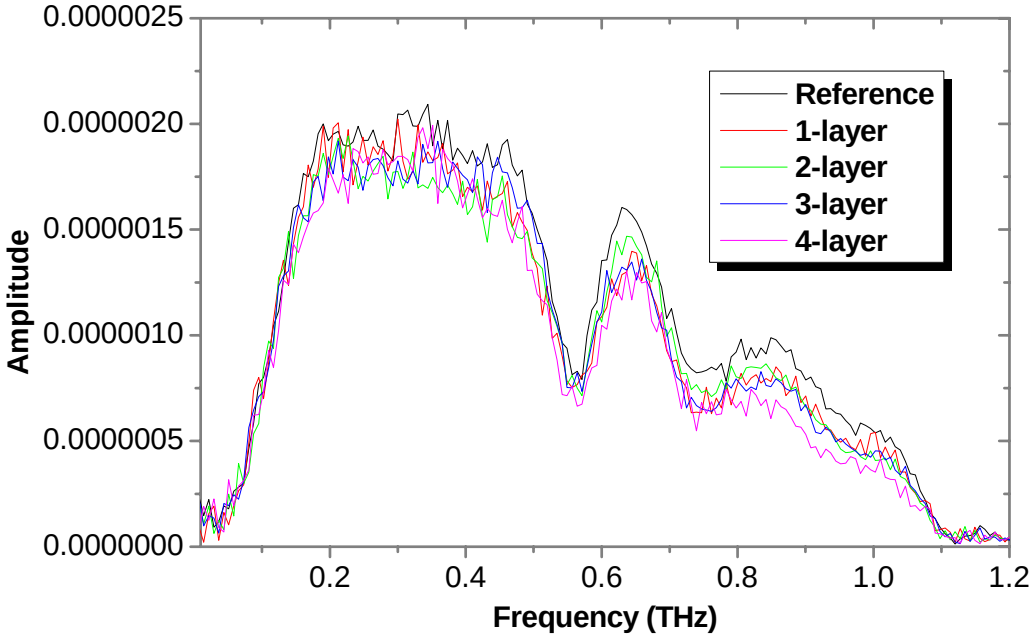

(b)

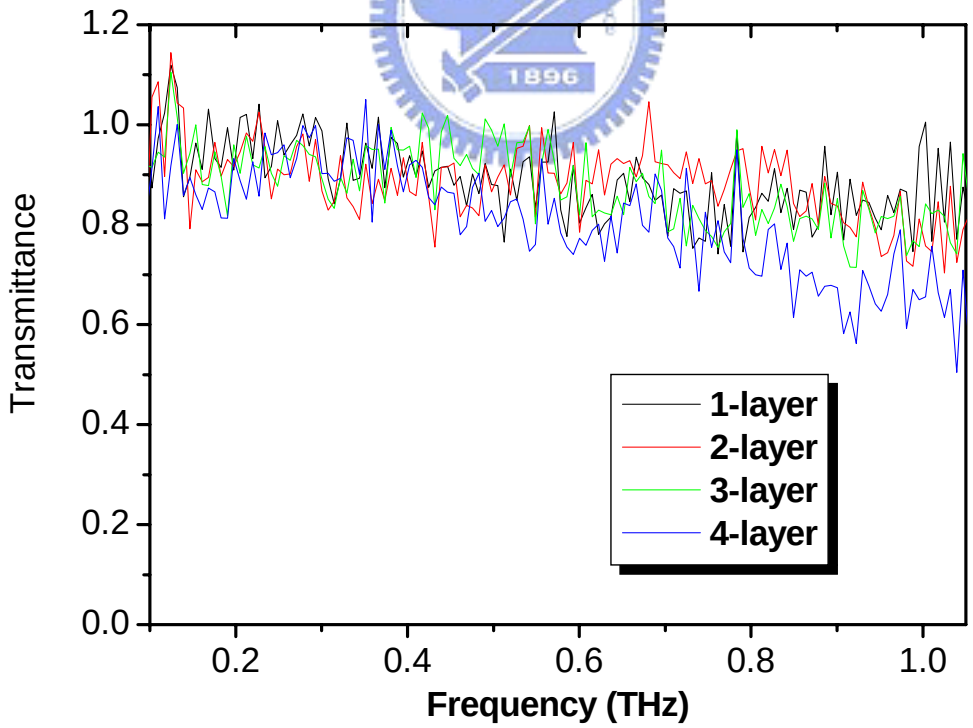

Fig. 4.13 Spectra and transmittances of 1-4 layers of tapes

(a)

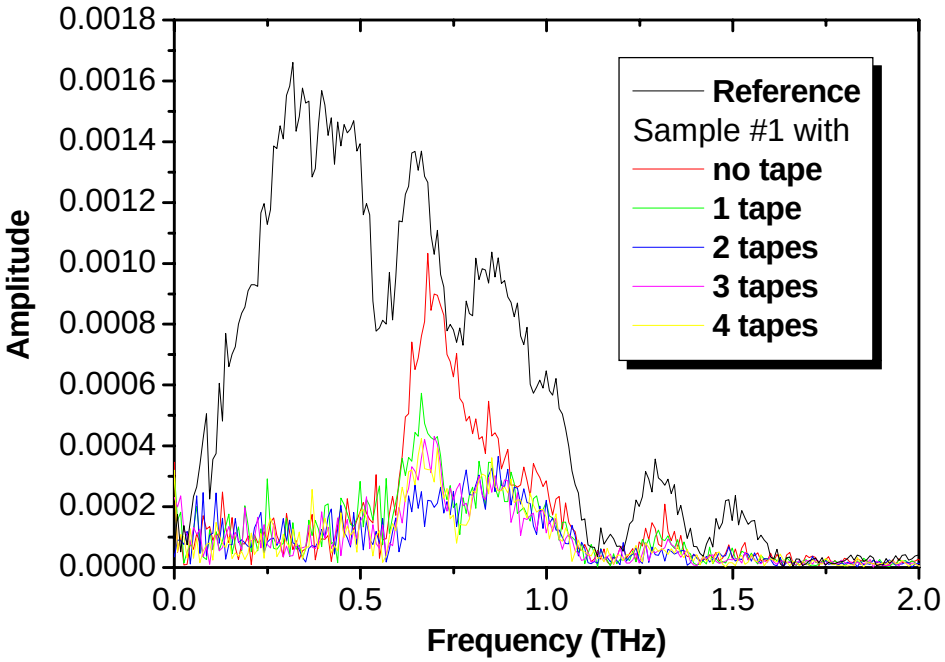

(b)

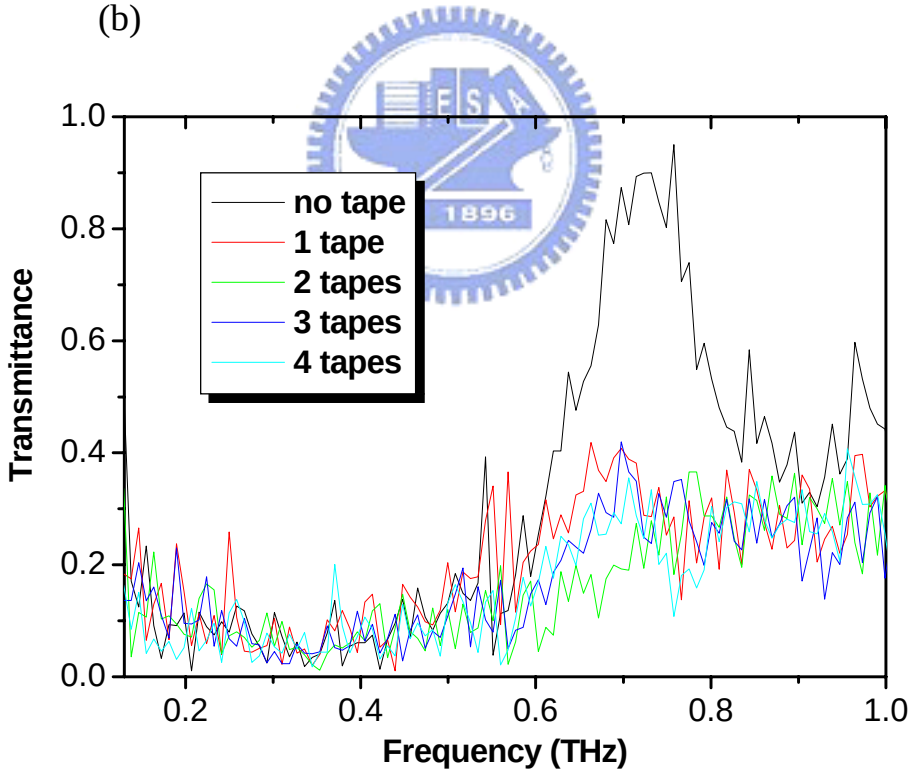

Fig. 4.14 (a) Spectra and (b) transmittance of Sample #1 with tapes on incident side

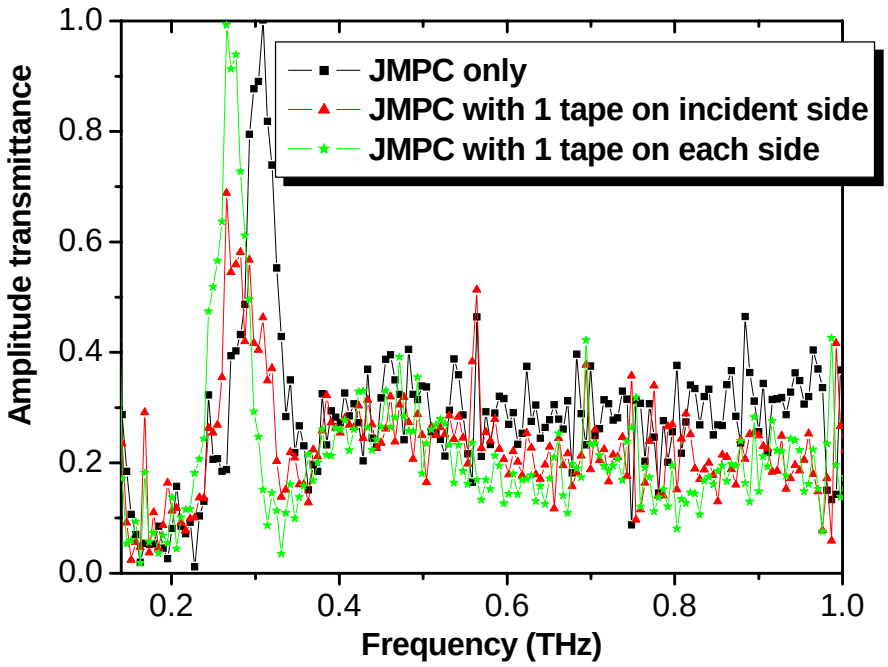

Fig. 4.15 Amplitude transmittance of JMPC with one tape on incident/each side

Table 4.2 Peak frequency and amplitude transmittance of JMPC with tapes on each side

Film thickness (μm)	υ_{peak} (THz)	$\Delta\upsilon/\Delta t_d$	T_A	T_n
0	0.309	NA	0.884	2.68
60	0.267	7E-4	0.711	1.73
120	0.240	5.75E-4	0.621	1.32
180	0.230	4.39E-4	0.444	0.67
240	0.230	3.29E-4	0.318	0.35

T_A: amplitude transmittance at peak frequency

T_n: normalized transmittance at peak frequency

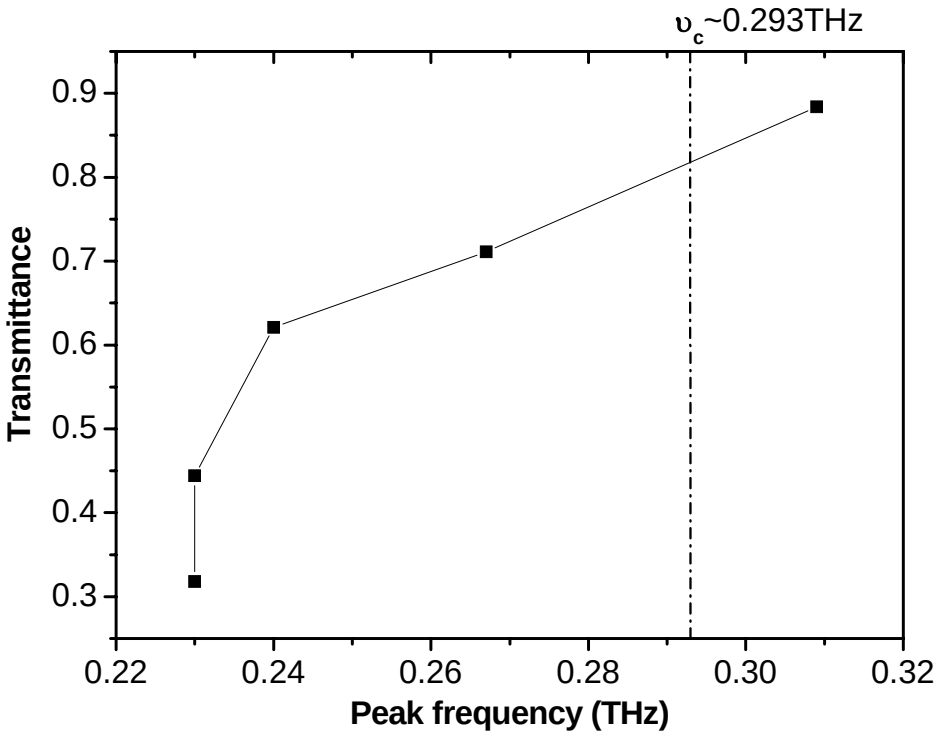

Fig. 4.16 Transmittance vs. peak frequency of JMPC with layers of tapes on each side

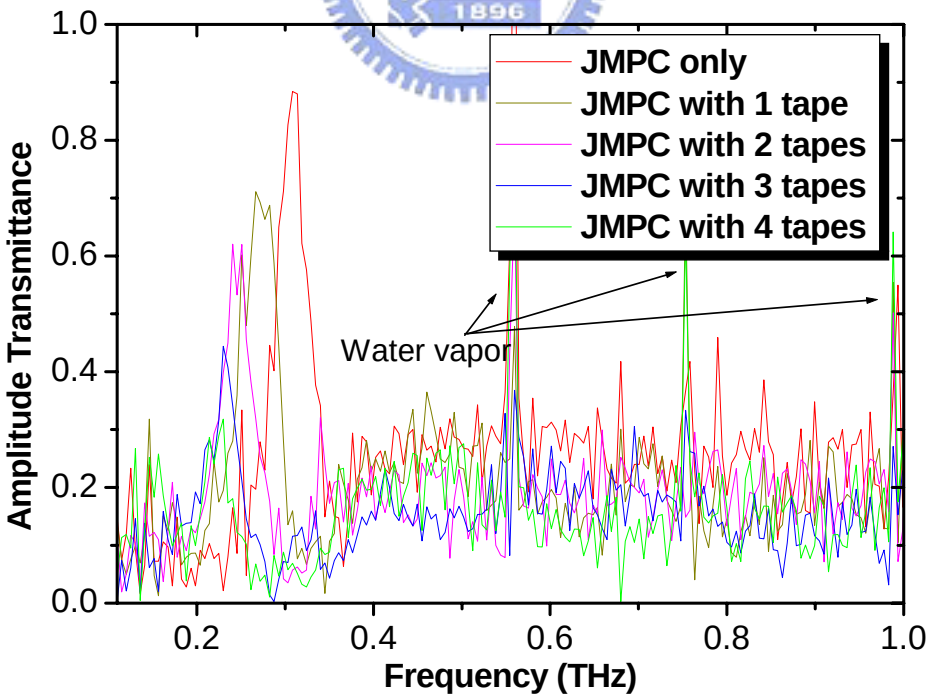

Fig. 4.17 Amplitude transmittance of JMPC with different layers of tapes on each side

due to the impedance matching and more obvious peak shifts owing to refractive index change, respectively.

From the results of Fig. 4.18, peak frequency shifts exponentially to lower frequency and peak frequency change is linearly decayed as the thickness of attached tapes was changed,. It could be due to increasing of the attenuation length with the thickness increasing.

Fig. 4.19 displays that normalized transmittance equals ~2.68 times of porosity at peak frequency of JMPC. Normalized transmittance of JMPC with 0 to 2 tapes (0-120 μm) shows larger than unity of porosity. Hence, extraordinary transmission occurs at some transmission frequencies of JMPC.

4.2.4 Fabry-Perot etalon made by two JMPCs with a cavity of ~ 0.5 mm spacing

A Fabry-Perot etalon as shown in Fig. 4.20 was fabricated by two JMPCs with a cavity of around 0.5 mm spacing. According to etalon effect, the 0.5 mm spacing corresponds to 0.3 THz and its higher-order harmonic frequencies. Fig. 4.21 shows the etalon effect makes the transmission peak sharper as the dash-dot circles indicated. Effect of a Fabry-Perot etalon with two mirrors replaced by MPCs is successfully accomplished.

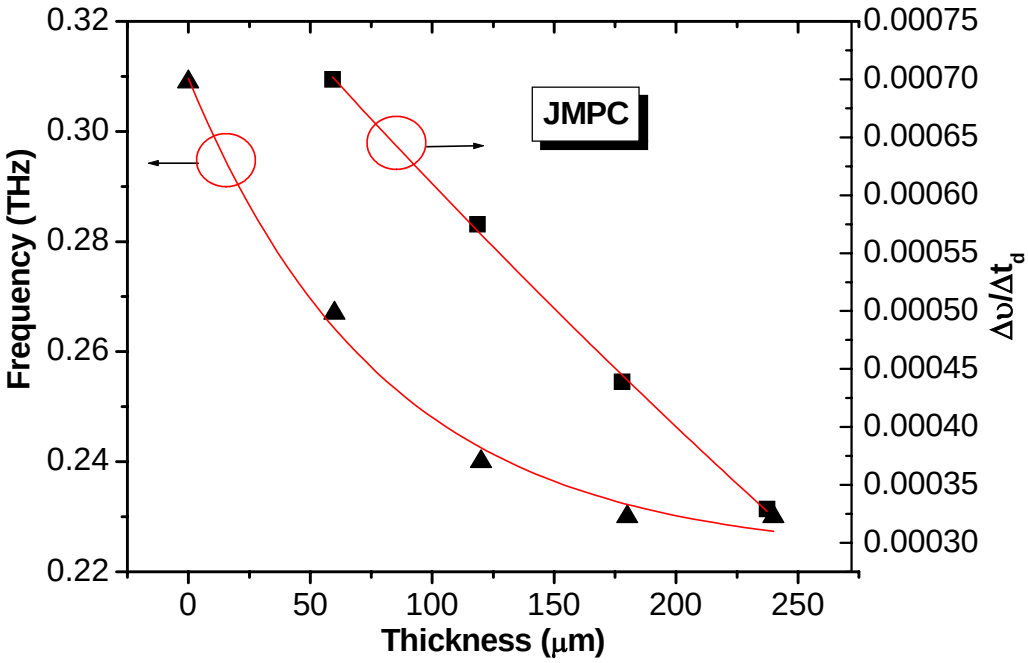

Fig. 4.18 Thickness change of tapes vs. peak frequency and its magnitude of shifts

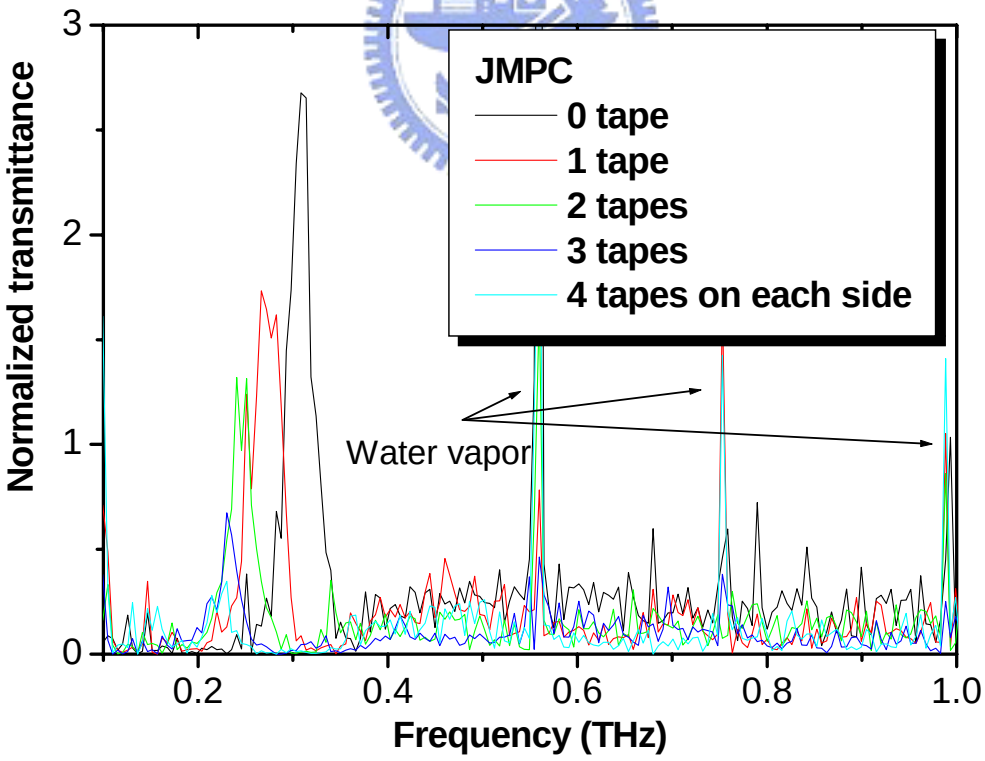

Fig. 4.19 Power transmittance normalized to porosity of JMPC with tapes attached to each side

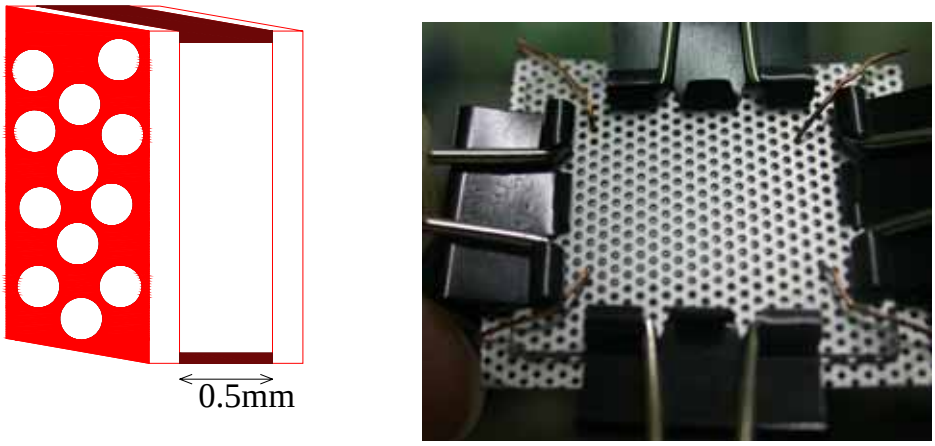

Fig. 4.20 Pictures of a Fabry-Perot etalon

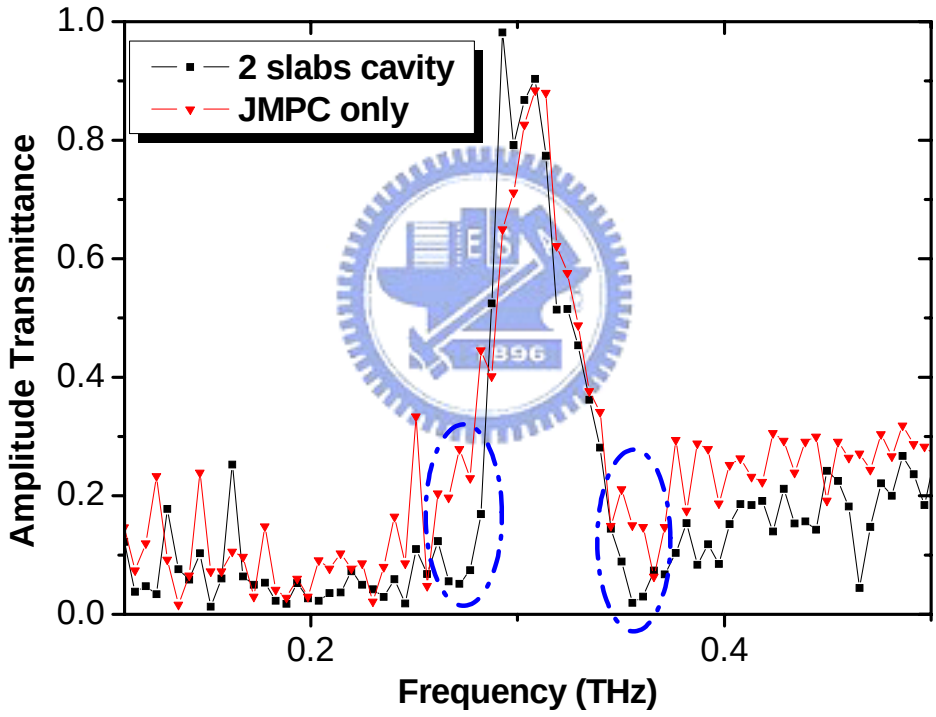

Fig. 4.21 Transmittance of a Fabry-Perot cell with a cavity of ~ 0.5mm spacing

5. Conclusions and Future Works

The transmission properties of metallic photonic crystals perforated with a triangular array of circular holes in THz region are known. Transmission band of MPCs can be well controlled by changing the three parameters of MPCs. Besides, 3M tapes shows no obvious absorption in 0.1~1THz. When they are attached to incident side of the MPCs, transmission bands of MPCs displays anomalous drop in a certain region. Furthermore, if they are attached on each side with equal layers of tapes, peak frequency of transmission band shifts to lower frequency below the cutoff. This phenomenon may be caused by refractive index change derived from surface plasmon theory. Finally, a Fabry-Perot cell of two MPCs is constructed. The results of this cell show shaper transmission band. It could be attributed to the Fabry-Perot effect.

In the future, effect of defect structures will be an interesting topic because it may have some large transmission peaks in the forbidden band. In addition, THz components of MPCs with tunable transmission band will be fabricated. To achieve this goal, liquid crystals (LCs) will be essential elements. Therefore, a MPC cell infiltrated with LCs can be made to change the transmission band by tuning the effective refractive index of LCs applied by magnetic field because metals of the MPCs in this study show no magnetic response.

Appendices

Appendix 1 Resolution in Sampling

Table A1 Time resolution vs. Frequency resolution for 1024 sampling points

Sampling delay step size (μm)	Time resolution (ps)[1]	Frequency Range (THz)[2]	Frequency Resolution (THz)[3]
4	0.02667	18.74	0.03653
5	0.03333	14.99	0.02922
6	0.04	12.499	0.02436
7	0.04667	10.708	0.02087
8	0.05333	9.37	0.01827
9	0.06	8.329	0.01624
10	0.06667	7.496	0.01461
11	0.07333	6.81477	0.01328
12	0.08	6.2469	0.01218
13	0.08667	5.76635	0.01124
14	0.09333	5.35447	0.01044
15	0.1000	4.9975	0.00974
16	0.10667	4.68	0.00912
17	0.11333	4.40956	0.0086
18	0.12	4.16458	0.00812
19	0.12667	3.9454	0.00769
20	0.13333	3.748	0.00731
26	0.17333	2.88317	0.00562
27	0.18	2.77639	0.00541
30	0.2001	2.49875	0.00487
33	0.22011	2.27159	0.00443
40	0.2668	1.87406	0.00365
42	0.28014	1.78482	0.00348

[1]Time Resolution (ps) = [Sampling Delay step size (μm) * 2] / Light Speed in vacuum 300 (μm /ps)

[2]Frequency Range (THz): Full positive frequency range after fast Fourier transform (FFT).

[3]Frequency Resolution (THz) = Frequency Range (THz)/ [1024 /2+1]

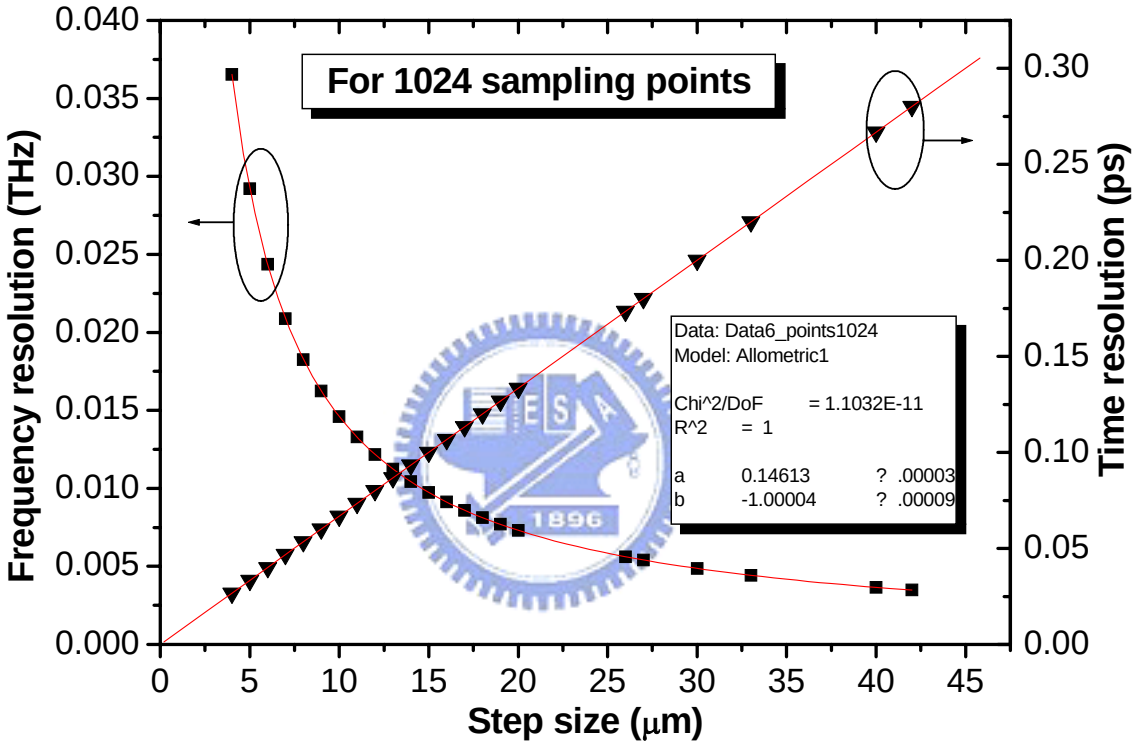

Fig. A1.1 Sampling step size vs. frequency and time resolution

Appendix 2 Etalon effect

Etalon effect is caused by multiple internal reflections when radiation passes through a parallel-sided material. The exiting light with numbers of internal reflections interferes so that fringes occur.

Assuming normal incidence and the material located in air (n=1), the electric field $E_t(\omega)$ of exiting light can be written as a function of electric field $E_i(\omega)$ of incident light:

$$E_t(\omega) = E_i(\omega)t_1t_2e^{i\omega t} + E_i(\omega)t_1t_2r_1r_2e^{i(\omega t-\delta)} + E_i(\omega)t_1t_2r_1^2r_2^2e^{i(\omega t-2\delta)} + \cdots \quad \text{(A2.1)}$$

where t_1, t_2 are transmission coefficients in 1st and 2nd interfaces, respectively:

$$t_1 = \frac{2n(\omega)}{n(\omega)+1}; t_2 = \frac{2}{n(\omega)+1},$$

r_1, r_2 are reflection coefficients in 1st and 2nd interfaces, respectively:

$$r_1 = r_2 = r = \frac{1-n(\omega)}{n(\omega)+1},$$

$n(\omega)$ is the frequency-dependent refractive index of the material, and δ is the phase difference induced by internal reflections:

$$\delta = 2n(\omega)d$$

where d is thickness of the material. Summed to infinity, the transmitted electric field can be reduced to:

$$E_t(\omega) = e^{i\omega t}\frac{E_i(\omega)t_1t_2}{1-r^2e^{i\delta}}. \quad \text{(A2.2)}$$

Multiplying $E_t(\omega)$ by its complex conjugate yields the irradiance of the exiting light:

$$I_t = I_i \frac{(t_1 t_2)^2}{(1+r^4) - 2r^2 \cos\delta} \qquad \text{(A2.3)}$$

If introducing the coefficient of finesse F such that

$$F \equiv \left(\frac{2r}{1-r^2}\right)^2,$$

The Eq. (A2.3) can be written as

$$\frac{I_t}{I_i} = \frac{1}{1+F\sin^2(\delta/2)}$$

The term $[1+F\sin^2(\delta/2)]^{-1} \equiv A(\theta)$ is known as an Airy function.

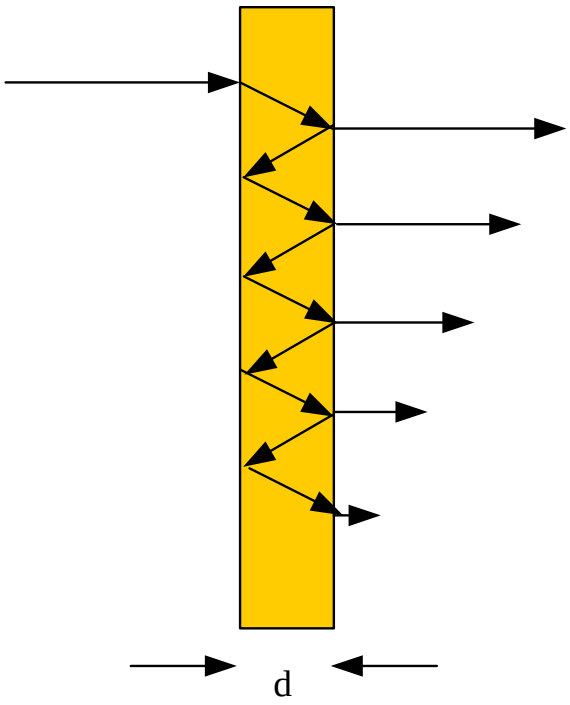

Fig. A2.1 Illustration of Fabry-Perot etalon effect

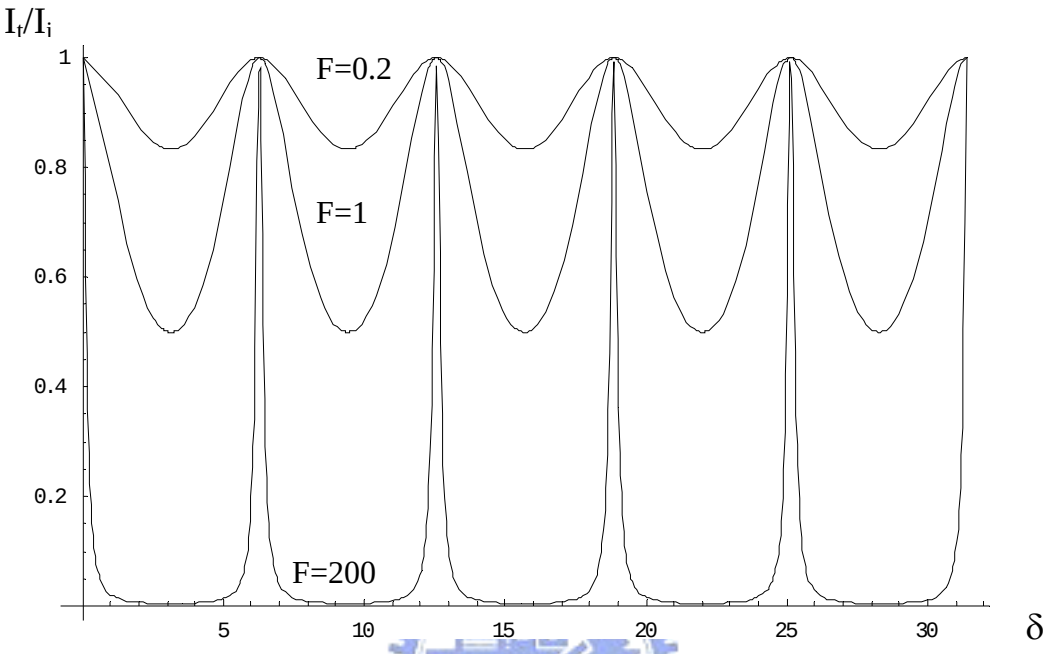

Fig. A2.2 Airy function

References

1. M. M. Sigalas, C. T. Chan, K. M. Ho, and C. M. Soukoulis, ”Metallic photonic band-gap materials,” *Phys. Rev. B*, vol. 52, no. 16, pp. 11 744-11 751, Oct. 1995
2. C. Y. Chen, T. R. Tsai, C. L. Pan, and R. P. Pan, “Room temperature terahertz phase shifter based on magnetically controlled birefringence in liquid crystals”, *Appl. Phys. Lett*., vol. 83, no. 22, pp. 4497-4499, Dec. 2003
3. F. Miyamaru, T. Kondo, T. Nagashima, and M. Hangyo, “Large polarization change in two-dimensional metallic photonic crystals in subterahertz region,” *Appl. Phys. Lett.*, vol. 82, no. 16, pp. 2568-2570. Apr. 2003
4. C. Winnewisser, F. T. Lewen, M. Schall, M. Walther, and H. Helm, “Characterization and Application of Dichroic Filters in the 0.1-3THz Region”, *IEEE Trans. Microwave Theory Tech.*, vol.48, no. 4, pp. 744-749, Apr. 2000
5. T. J. Yen, W. J. Padilla, N. Fang, D. C. Vier, D. R. Smith, J. B. Pendry, D. N. Basov, X. Zhang, “Terahertz Magnetic Response from Artificial Materials,” *Science*, vol. 303, pp. 1494-1496, Mar. 2004
6. T. W. Ebbesen, H. J. Lezec, H. F. Ghaemi, T. Thio, and P. A. Wolff, “Extraordinary optical transmission through sub-wavelength hole arrays,” *Nature*, vol. 391, pp. 667-669, Feb. 1998
7. Mourou G, Stancampiano C V, Antonetti A and Orszag A, “Picosecond microwave pulse generation,” *Appl. Phys. Lett*., vol. 38, no. 6, pp. 470-472, Mar. 1981
8. Auston D H, Cheung K P and Smith P R, “Picosecond photoconducting Hertzian dipoles,” *Appl. Phys. Lett.*, vol.45, no. 3, pp. 284-286, Aug. 1984
9. Q. Wu and X. –C. Zhang, “Ultrafast electro-optic field sensors”, *Appl. Phys. Lett.*, vol. 68, no.12, pp. 1604-1606, Mar.1996
10. D. Dragoman, M. Dragoman, “Terahertz fields and applications,” *Pro. in Quantum Electron.*, vol. 28, no. 1, pp. 1-66, 2004
11. L. Xu, X.-C. Zhang, and D. H. Auston, ”Terahertz beam generation by femtosecond optical pulses in eletro-optic materials,” *Appl. Phys. Lett.*, vol 61, no. 15, pp. 1784-1786, Oct. 1992
12. P. Uhd Jepsen, R. H. Jacobsen, and S. R. Keiding, “Generation and detection of terahertz pulses from biased semiconductor antennas,” *J.*

Opt. Soc. Am. B, vol. 13, no. 11, pp. 2424-2436, Nov. 1996
13. M. van Exter, Ch. Fattinger, and D. Grischkowsky, "Terahertz time-domain spectroscopy of water vapor," *Opt. Lett.*, vol. 14, no. 20, pp. 1128-1130, Oct. 1989
14. C. Ronne, P. Astrand, and S. R. Keiding, "THz Spectroscopy of Liquid H_2O and D_2O," *Phys. Rev. Lett.*, vol. 82, no. 14, pp. 2888-2891, Apr. 1999
15. M. Walther, K. Jensby, and S. R. Keiding, H. Takahashi and H. Ito, "Far-infrared properties of DAST," *Opt. Lett.*, vol. 25, no. 12, pp. 911-913, June 2000
16. D. Grischkowsky, S. Keiding, M. van Exter, and Ch. Fattinger, "Far-infrared time-domain spectroscopy with terahertz beams of dielectrics and semiconductors", *J. Opt. Soc. Am. B*, vol.7, no. 10, pp. 2006-2014, Oct. 1990
17. B. B. Hu and M. C. Nuss, "Imaging with terahertz waves," *Opt. Lett.*, vol. 20, no. 16, pp. 1716-1718, Aug. 1995
18. D. M. Mittleman, R. H. Jacobsen, and M. C. Nuss, "T-Ray Imaging," *IEEE J. Selected Topics in Quantum Electron.*, vol. 2, no. 3, pp. 679-692, Sep. 1996
19. M. Herrmann, M. Tani, and K. Sakai, "Terahertz imaging of silicon wafers," *J. Appl. Phys.*, vol.91, no. 3, pp.1247-1250, Feb. 2002
20. P. Y. Han, G. C. Cho, and X.-C. Zhang, "Time-domain transillumination of biological tissues with terahertz pulses", *Opt. Lett.*, vol. 25, issue 4, pp. 242-244, Feb. 2000
21. A. J. Fitzgerald, E. Berry, N. N. Zinovev, G. C. Walker, M. A. Smith, and J. M. Chamberlain, "An introduction to medical imaging with coherent terahertz frequency radiation," *Phys. Med. Biol.*, vol.47, R67-R84, Mar. 2002
22. http://www.frascati.enea.it/THz-BRIDGE/main.htm
23. C. -C. Chen, "Transmission of Microwave through Perforated flat plates of finite thickness," *IEEE Trans. Microwave Theory Tech.*, vol. MTT-21, no.1, pp. 1-5, Jan. 1973
24. H. Raether, "Surface plasmons on smooth and rough surfaces and on gratings," *Springer*, German 1988
25. R. H. Ritchie," Plasma Losses by Fast Electrons in Thin Films," *Phys. Rev.*, vol. 106, no. 5, pp. 874-881, June 1957
26. T. Thio, H. F. Ghaemi, H. J. Lezec, P. A. Wolff, and T. W. Ebbesen, "Surface-plasmon-enhanced transmission through hole arrays in Cr

films,” *J. Opt. Soc. Am. B*, vol.16, no. 10, pp. 1743-1748, Oct. 1999
27. M. van Exter, Ch. Fattinger, and D. Grischkowsky, “Terahertz time-domain spectroscopy of water vapor,” *Opt. Lett.*, vol.14, no. 20, pp. 1128-1130, Oct. 1989
28. N. N. Markina, A. P. Naumov, and A. V. Troitskij,” Emission and absorption of impurity gases in the lower atmosphere,” *Proc. SPIE Millimeter and Submillimeter Waves II*, vol. 2558, pp. 201-208, Oct. 1995